Measurement of the g-factor anisotropy in a lateral GaAs spin qubit

Master's Thesis, University of Basel

Supervisors: Prof. Dr. Dominik Zumbühl & Dr. Leon Camenzind

Second reviewer: Dr. Christian Scheller

Simon Svab

26.09.2019

Universität
Basel

Philosophisch-Naturwissenschaftliche
Fakultät

Erklärung zur wissenschaftlichen Redlichkeit

(beinhaltet Erklärung zu Plagiat und Betrug)

~~Bachelorarbeit~~ / Masterarbeit *(nicht Zutreffendes bitte streichen)*

Titel der Arbeit *(Druckschrift)*:

Measurement of the g-factor anisotropy in a lateral
GaAs spin qubit

Name, Vorname *(Druckschrift)*: Svab, Simon

Matrikelnummer: 14-051-924

Hiermit erkläre ich, dass mir bei der Abfassung dieser Arbeit nur die darin angegebene Hilfe zuteil wurde und dass ich sie nur mit den in der Arbeit angegebenen Hilfsmitteln verfasst habe.

Ich habe sämtliche verwendeten Quellen erwähnt und gemäss anerkannten wissenschaftlichen Regeln zitiert.

Diese Erklärung wird ergänzt durch eine separat abgeschlossene Vereinbarung bezüglich der Veröffentlichung oder öffentlichen Zugänglichkeit dieser Arbeit.

☐ ja ☒ nein

Ort, Datum: Basel, 26.9.2019

Unterschrift: Simon Svab

Dieses Blatt ist in die Bachelor-, resp. Masterarbeit einzufügen.

Januar 2017

Abstract

Spin qubits constitute one of the most promising platforms for large-scale quantum computation due to their inherent potential to be scalable to a large number of qubits and their small size. In this thesis, the successful experimental measurement of the g-factor anisotropy in a lateral GaAs single-electron spin qubit device is presented. While applying an in-plane magnetic field of varying strength and direction, the Zeeman splittings are extracted by measuring the tunneling rates into the individual spin states of the empty quantum dot. The results are compared with a recent theoretical model, which separates the corrections to the bulk g-factor of GaAs into isotropic and anisotropic contributions that originate from different spin-orbit interaction terms. By varying the direction of the magnetic field, values between $|g| \approx 0.365$ and $|g| \approx 0.415$ are obtained. From the measurements in this device, the determined anisotropic correction $\delta g_a \approx 0.025$ is in good agreement with the theory. The isotropic correction reduces the average g-factor below the GaAs bulk value $|g| = 0.44$ to an average g-factor $|\bar{g}| \approx 0.396$, corresponding to an isotropic correction $\delta g_i \approx 0.044$ which is weaker than predicted by the theory. These results could help determining the relevant parameters from $\mathbf{k} \cdot \mathbf{p}$ theory with an increased accuracy. Furthermore, the observation that the spin splitting changes with the direction of the magnetic field is of high significance for the addressability and operation of a spin qubit. Thus, the findings presented in this thesis will allow for the further optimization of spin qubits in the future.

The results of the work presented in this thesis have been published as a part of Ref. [1].

Table of contents

1 Introduction

As a major milestone of technological progress, the advances in solid-state physics that were made in the 20th century paved the way for the semiconductor industry, which revolutionized electronics in the 1960s and thereby started the new era of the information age. Moore's law [2], stating that the number of transistors on an integrated circuit grows exponentially in time, was fulfilled from the start of chip mass production in the 1970s until the early 2010s. Transistors have become an order of magnitude smaller, with node sizes changing from a few μm in the 1970s to the current standard of a few nm - a size regime where quantum effects become more important. As the downscaling of transistors becomes increasingly difficult, a saturation in the growth of transistor counts has been observed in recent years.

In the 1980s, the concept of a quantum computer was outlined, representing a platform that could efficiently simulate and solve quantum mechanical problems [3]. In a simplified picture, a classical computer takes an input in the form of a string of binary bit values of 0 or 1 and performs predefined mathematical operations using logical gates on it, which produces an output that again takes on the form of a bit string. In analogy to a classical computer, the basic building block of a quantum computer is the qubit, which represents a quantum two-level system that is in a superposition of basis states 0 and 1. In the circuit model, a quantum computer converts a binary input to a qubit state and applies quantum gates in order to generate any unitary transformation. After a projective measurement, the qubit state collapses and a classical binary output is returned. There are several potential applications for quantum computers. For example, several quantum algorithms have been proposed with which certain problems could be solved faster and where the scaling with size would be more favourable than with a classical computer. Furthermore, it is predicted that quantum computers could help solving complex problems in quantum chemistry in order to discover, for example, new medicines.

To help selecting suitable physical systems that could be used as qubits, the five DiVincenzo criteria [4] were postulated: i.) the qubits must be scalable, ii.) it must be possible to initialize the qubits in a known state, iii.) the decoherence time of the qubits must be much longer than the gate operation times, iv.) a universal set of quantum gates can be implemented and v.) it must be possible to measure the result of a computation on specific qubits.

The system that is investigated in this thesis closely resembles the original proposal of the so-called Loss-DiVincenzo qubit [5]. It is realized in a heterostructure consisting of the III-V compound semiconductors gallium arsenide (GaAs) and aluminum gallium arsenide (AlGaAs). At the GaAs-AlGaAs interface, a two-dimensional electron gas (2DEG) can be formed, which confines the electrons in the direction perpendicular to the interface and results in a finite electron density and high electron mobility in the two-dimensional plane that is parallel to the interface. In order to reach the quasi zero-dimensional confinement of a quantum dot, negative voltages are applied to gates which are located on the surface of the device. The resulting electric field depletes the regions in the 2DEG which are situated underneath these gates and, using certain gate geometries, a quantum dot can be formed which contains only a few electrons. The electrons tunnel in and out of the quantum dot from reservoirs on its side, and hence such a geometry is referred to as a lateral quantum dot.

Owing to their large charge carrier mobilities, a substantial part of the experimental groundwork for the realization of spin qubits such as successful confinement [6], charge sensing [7], single-shot readout [8, 9] and the realization of quantum gates [10, 11] has been first carried out in GaAs 2DEG systems. In this thesis, a GaAs/AlGaAs lateral single-electron quantum dot spin qubit device is investigated. Upon applying an in-plane magnetic field, the quantized energy levels in the quantum dot split according to the Zeeman splitting $\Delta E_Z = g \cdot \mu_B \cdot B$, where g is the g-factor, $\mu_B \approx 58$ μeV/T the Bohr magneton and B

the applied magnetic field. For the discussed device type, a recent theoretical model by Stano et al. [12] predicts deviations of the electron g-factor from that of the bulk material which originate from spin-orbit interaction (SOI) effects. The strength of these corrections depend on the thickness l_z of the quantum dot wave function in the direction perpendicular to the 2DEG plane. Notably, one of the dominating corrections to the g-factor stems from the Dresselhaus SOI, which originates from the inversion asymmetric Zincblende crystal structure of GaAs and exhibits an anisotropy in the plane of the 2DEG. Due to this effect, it is expected that a g-factor anisotropy of approximately 10%, depending on the direction of the in-plane magnetic field, can be observed. Here, the anisotropic correction from the Dresselhaus SOI is on the same order as isotropic correction terms that result from other SOI mechanisms, which results in a strong g-factor anisotropy compared to some other materials. For example, measurements of the g-factor anisotropy in silicon quantum dots have shown an anisotropy of only 2% [13], owing to the bulk-inversion symmetric diamond crystal structure of the host material. Indeed, measurements on a first GaAs device have shown a g-factor anisotropy that is in agreement with the theoretical predictions [1]. In this thesis, the measurements on a second device of the same type, which was fabricated on a slightly different wafer, are presented.

Several aspects that motivate this work are related to the spin-relaxation time T_1 and the coherence time T_2. In connection with the third DiVincenzo criterion, both of these times have a high significance for the successful operation of a qubit. In GaAs, a T_1 reaching tens of seconds has been measured: On the same device where the preliminary g-factor anisotropy was measured, Camenzind et al. [14] previously determined a spin relaxation time $T_1 = 57 \pm 15\ s$, setting the world record for an electron spin lifetime in a nanostructure. Holding relevance for the g-factor anisotropy measurements, a dependence of the spin relaxation time on the Zeeman splitting, $T_1 \propto \Delta E_Z{}^{-5}$ has been predicted in theory [15] and shown experimentally [16]. With such a strong dependence, knowledge over the anisotropy of the g-factor can in principle allow control over qubit parameters such as T_1.

In contrast to the long spin relaxation times in GaAs quantum dots, the measured coherence times T_2 were only on the order of tens of nanoseconds [10, 11]. In GaAs, T_2 is limited by the hyperfine interaction that results from the effective magnetic field of surrounding nuclear spins in the host material with the electron spin. Because the dynamics of the nuclear spin bath are comparably slow, these short coherence times can be improved with decoupling procedures, which increase T_2 to a value that is close to 1 ms [17]. In this time regime, the decoherence time may also be impaired by charge noise, which results from random charge fluctuations in the wafer material. The charge noise causes the confinement potential to fluctuate, thereby changing the position of the wave function. When g changes with the position of the wave function, ΔE_Z is also changed as a result. Since the electron spin resonance frequency $f_{ESR} = \frac{\Delta E_Z}{h}$ is a key ingredient for the addressability of the qubit [18], fluctuations in ΔE_Z are connected to a loss in coherence times [19, 20]. Further insight on spatial variations of the g-factor could help addressing this issue. Finally, the g-factor is a very fundamental quantity, and an experiment such as the one discussed in this thesis can help to better understand the underlying physics. From the experimental data presented here, material-specific spin-orbit parameters could be extracted, thereby supporting further theoretical investigations.

There have been a number of experiments that investigated the electron g-factor in GaAs quantum dots. On a similar heterostructure as the one investigated in this thesis (with the 2DEG situated approximately 100 nm below the surface), Potok et al. [21] measured $|g| \approx 0.37$ for a single-electron quantum dot through transport spectroscopy over a magnetic field range of 0 to 6 T, deviating from the GaAs bulk g-factor of -0.44. Using a quantum point contact as a charge sensor for transport through the quantum dot, Hanson et al. [22] measured a nonlinear deviation from the bulk g-factor at magnetic fields above 5 T, which was attributed to the magnetic field pushing the electron wave function into the neighbouring AlGaAs region at high fields. Investigations of the Kondo effect in GaAs quantum dots also allowed to extract the g-factor, yielding values of $|g| \approx 0.29$ [23] and $|g| \approx 0.15$ [24] for more shallow 2DEGs (situated approximately 15 nm below the surface), and $|g| \approx 0.44$ [25] for a 2DEG depth of approximately 100 nm. In a similar heterostructure, the angular dependence of the single-electron g-factor in the 2DEG plane was investigated by Zumbühl et al. [26] in 2004, yielding values around $|g| \approx 0.4$. However, the uncertainty around ±15% of the g-factor was too large to observe the smaller g-factor anisotropy. In a more recent experiment, Michal et al. [27] measured the g-factor in several arrays of GaAs quantum dots for different magnetic field directions by means of electric dipole spin resonance (EDSR). In line with their predictions, they obtained $|g| \approx 0.36$ along the $[1\,1\,0]$ crystal direction for a double dot, and $|g| \approx 0.44$ along the $[1\,\bar{1}\,0]$ direction for a triple dot and a quadruple dot.

This thesis is structured as follows: In chapter 2, the basic physics of a GaAs spin qubit device and the theoretical predictions for the g-factor corrections in such a device are presented. In chapter 3, the measurement methods for this work are outlined. Finally, the experimental results are presented in chapter 4, showing that it was indeed possible to successfully measure the g-factor anisotropy in the course of this thesis.

2 Theoretical background

In this chapter, the underlying physics of GaAs spin qubits is discussed. First, the heterostructure system which was used to fabricate the device is described. Then, the concept and basic principles of quantum dots are introduced. Following this, a brief description of the important types of spin-orbit interaction is given. Spin-orbit interactions are a key component for the theoretical predictions of the g-factor corrections, which are shown in the last section of this chapter.

2.1 The two-dimensional electron gas

The device that was investigated in this thesis is hosted on a GaAs/AlGaAs heterostructure. GaAs is a III-V compound semiconductor that crystallizes in zincblende structure, which can be thought of as two displaced face-centered cubic sublattices of Ga and As atoms. The zincblende structure has a tetrahedral symmetry, and as such possesses no inversion center. This asymmetry of the bulk material gives rise to spin-orbit effects which will be discussed later in this chapter. By partial substitution of the Ga atoms with the group III Al atoms, the band gap energy can be tuned between the value of GaAs ($E_{g,GaAs}$= 1.44 eV) and the value of AlAs ($E_{g,AlAs} = 2.16$ eV). This alloy can be written as $\mathrm{Al}_x\mathrm{Ga}_{1-x}\mathrm{As}$, where x describes the Al concentration and can take a value between 0 and 1. For the heterostructure that is described here, a frequently used Al concentration of x = 0.3 was used, and following mentions of AlGaAs will refer to this concentration. GaAs and AlAs have a very small mismatch within 0.5% of their lattice constant, thus allowing the formation of strain-free GaAs/AlGaAs interfaces.

An overview of the wafer profile is given in Fig. 1, showing the different layers that are grown on the GaAs bulk crystal using molecular-beam epitaxy. At the interface between GaAs and AlGaAs, a heterojunction is formed due to the difference in band gap energies. Due to an n-type silicon δ-doping layer situated 40 nm above the heterojunction, a triangular quantum well forms at the GaAs/AlGaAs interface. Here, the donated electrons are electrostatically drawn to the ionized dopant atoms yet unable to surpass the interface at low enough temperatures, resulting in a linear electric field that gives the triangular confinement. Inside the confinement potential, the energy states are quantized and form sub-bands. For the wafers discussed in this thesis, a temperature below approximately 100 K causes the electrons to only occupy the lowest sub-band. In this limit, the strong confinement will prevent movement of the electrons in the direction that is perpendicular to the interface, which is here denoted as z. Due to this strong confinement in one direction, such a system is referred to as a two-dimensional electron gas (2DEG). This system shows a high electron mobility, which is a result of the strain-free nature of the GaAs/AlGaAs interface and the remote doping that brings ionized donors out of the direct path of the electrons. To increase the mobility even further, a GaAs/AlGaAs superlattice, totalling to 100 nm, is placed between the GaAs bulk crystal and the 800 nm GaAs layer hosting the 2DEG. The superlattice consists of periodically spaced 3 nm GaAs and 3 nm AlGaAs layers and leads to a further reduction of the strain. On top of the heterostructure, a 10 nm GaAs capping layer is grown to avoid oxidation of the Al atoms in the underlying AlGaAs. On this capping layer, Ti/Au surface gates are deposited. By applying negative voltages to these gates, regions in the underneath 2DEG are depleted of electrons. Using a suitable surface gate design in combination with the 2DEG properties, it is therefore possible to achieve the confinement that is necessary for such a lateral quantum dot.

The 2DEG represents one of the best experimental realizations of a two-dimensional system and the underlying physics has been well outlined in the literature (see e.g. Ref. [29]). In the plane of the 2DEG, the dispersion relation resembles that of a free electron, but with a different effective mass m^*:

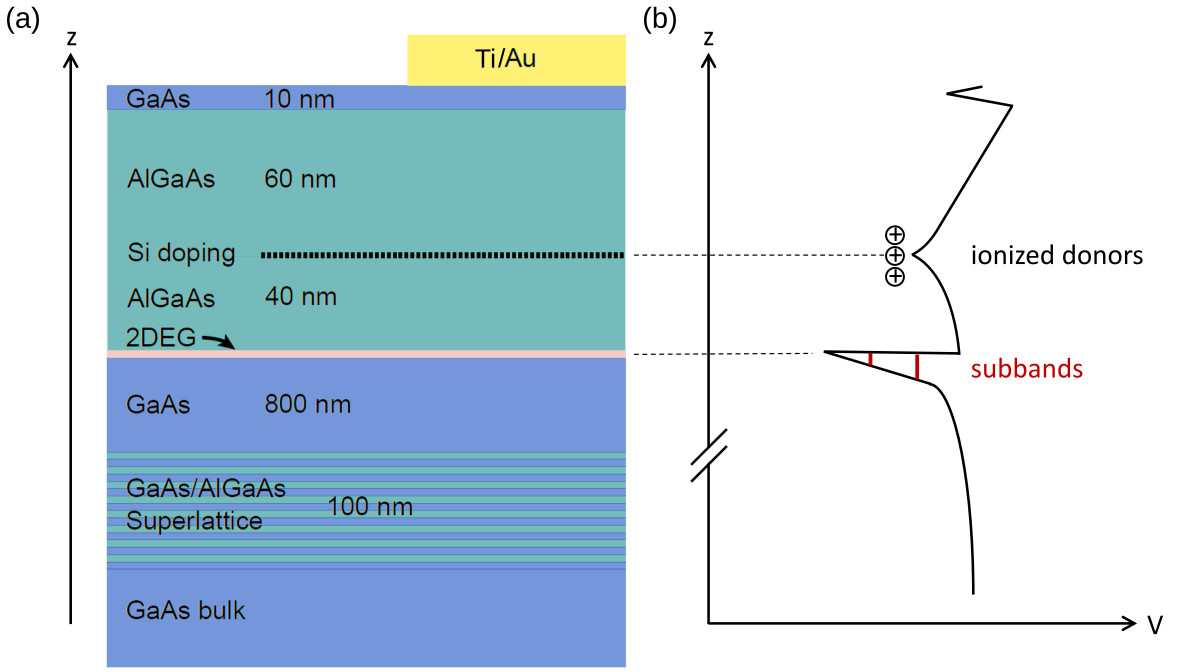

Figure 1: (a) Schematic cross section of the GaAs/AlGaAs heterostructure used in the experiment. The growth direction is denoted as z. 110 nm below the surface, a two-dimensional electron gas (2DEG) is formed at the GaAs/AlGaAs interface. The Ti/Au gates which are fabricated on top of the heterostructure serve to locally deplete the 2DEG underneath them. Adapted from Ref. [28].(b) Qualitative sketch of the potential V in the growth direction z. The Si dopants are ionized and remotely donate electrons to the 2DEG, which leads to the triangular shape of the quantum well with subbands shown in red.

$$E = \frac{\hbar^2 k^2}{2m^*}, \tag{1}$$

where $\hbar$ is the reduced Planck constant, k the wave vector and m^* the effective mass. For the conduction band in GaAs, $m^* = 0.067 m_e$, where m_e is the mass of the free electron. From the parabolic dispersion relation, a density of states,

$$\rho_{2D}(E) = \frac{g_s g_v m^*}{2\pi\hbar^2}, \tag{2}$$

can be calculated. For GaAs, $g_s = 2$ describes the degree of spin degeneracy and $g_v = 1$ the valley degeneracy of the conduction band minima, thereby reducing the density of states to $\rho_{2D}(E) = \frac{m^*}{\pi\hbar^2}$. Notably, the density of states for the 2DEG is independent of the energy.

2.2 Quantum dots

The accumulation of a few charge carriers in a quasi zero-dimensional confinement leads to interesting physics as electron-electron interactions become more important and the coupling to the environment becomes weaker [29]. Such objects are referred to as quantum dots. There are several different implementations of quantum dots, such as self-assembled quantum dots [30], vertical quantum dots [31], or lateral quantum dots which are the focus of this thesis. After discussing the gate layout and operation of a lateral quantum dot device, this section gives a qualitative introduction to the Coulomb blockade effect, which is a fundamental part of quantum dot physics. Due to the high significance for this thesis, the utilization of an adjacent quantum dot as a charge sensor is also briefly discussed.

2.2.1 Lateral quantum dots

In GaAs quantum dot devices, a quantum dot can be formed by applying negative voltages to gates on the device surface, thereby depleting the 2DEG that is formed at the heterostructure interface underneath. A scanning electron microscope image depicting the gate layout of the device that was investigated in this thesis is shown in Fig. 2a. The gates are labelled according to their functionality: Two wall gates (LW, RW) flanking the dot from the sides, a nose gate (N) and three plunger gates (LP, CP and RP) constitute the main confinement of the quantum dot. Furthermore, two separation gates (SEP) serve to form pointy reservoirs that are separated from the rest of the 2DEG. Beyond each of the two wall gates, a set of three further gates can be used to form a sensor quantum dot. This allows for a non-invasive measurement of the states in the main quantum dot.

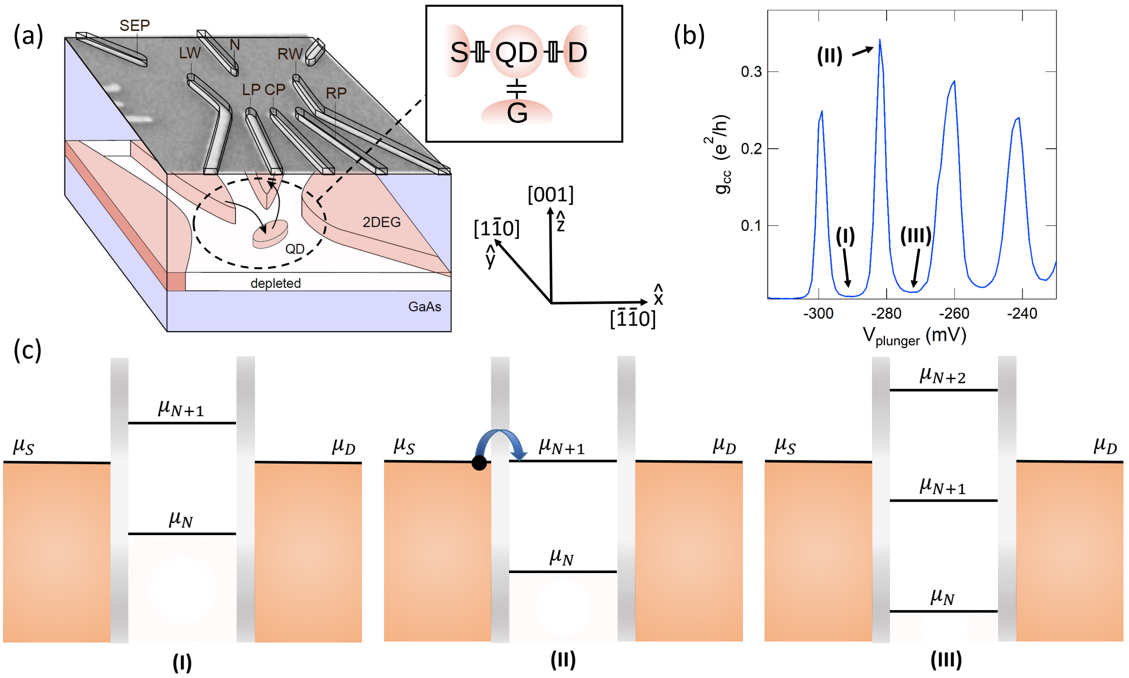

Figure 2: (a) Scanning electron micrograph of the device used for the experiments with an underlying schematic of the 2DEG. Due to the gate design, a quantum dot can be energized in the center. Inset: The quantum dot (QD) is tunnel coupled to the source (S) and drain (D) reservoirs and capacitively coupled to the gates (G). Adapted from Ref. [28]. (b) Measured Coulomb blockade peaks. Points corresponding to the configurations shown in (c) are marked (I)-(III). (c) Diagram representing transport through the quantum dot in the case where no bias voltage is applied, i.e. $\mu_S = \mu_D$. At configuration (I), the chemical potential μ_N for the quantum dot hosting N electrons lies below the reservoir chemical potentials while μ_{N+1} for the next electron lies above them, such that the occupation of the quantum dot remains fixed. In this configuration, transport through the quantum dot is prevented and the system is in Coulomb blockade. As the plunger gate voltage $V_{plunger}$ is made less negative, the chemical potential in the quantum dot is lowered until configuration (II) is reached. Here, the chemical potential μ_{N+1} of the (N+1)-electron state is in resonance with the reservoir potentials, thus allowing elastic tunneling in and out of the quantum dot. As $V_{plunger}$ is made even less negative, the system reenters Coulomb blockade which is shown in configuration (III).

The described gate layout allows for the manipulation of the shape and size of the main quantum dot. For example, all gate voltages can be uniformly made more negative, whereupon the quantum dot becomes smaller. In principle, this design also allows to squeeze the quantum dot in one direction, for example by making the plunger and nose gates more negative while compensating with less negative wall gates. For the device investigated in this thesis, such shape manipulation was not possible over significant ranges because the distances between gates led to a narrow parameter space of stable quantum dot configurations. More specifically, the gates at the center quantum dot were closer together than in the first device of Ref. [1, 32], such that they pinched off at less negative voltages.

2.2.2 Coulomb blockade effect

The energy level structure of a quantum dot is characterized by two energy scales: the charging energy and the confinement energy. The charging energy describes the electrostatic repulsion between electrons inside the quantum dot. Following the derivation in Ref. [29], it can be estimated as the capacitive charging energy of a disc with radius r that carries the charge $-|e|N$ (of N electrons in the dot) while surrounded by a material with the dielectric constant ϵ, giving a capacitance $C = 8\epsilon\epsilon_0 r$ and leading to the charging energy

$$E_c = \frac{e^2}{C} = \frac{e^2}{8\epsilon\epsilon_0 r}, \tag{3}$$

which is needed to add an additional electron to the quantum dot. From Eq. 3, it can be seen that the charging energy increases as the size of the quantum dot becomes smaller. Such a treatment is valid under the constant interaction model [16], which is based on two assumptions: First, the interactions of electrons in the dot with other electrons in the dot and electrons in the environment of the dot can be parametrized by a single capacitance C_{tot}, such that

$$C_{tot} = C_S + C_D + C_G. \tag{4}$$

This is a sum of capacitances between the quantum dot and the source reservoir C_S, the drain reservoir C_D and the gates C_G. As a second requirement for the model, it is assumed that the energy level spacing due to the confinement is not affected by interactions of the electrons and thus independent of the electron number.

The confinement energy for a few-electron quantum dot with a harmonic confinement potential of radius r and effective mass m^* can be estimated as a quantum harmonic oscillator with a frequency $w_0 = \frac{\hbar}{4r^2 m^*}$ [29], leading to the orbital spacing

$$\Delta = \hbar w_0 = \frac{\hbar^2}{4r^2 m^*}. \tag{5}$$

Both the relative strength of the charging energy and the confinement energy depend on the size of the quantum dot. For small, self-assembled quantum dots with a radius below the Bohr radius a_B^*, the confinement energy is larger than the charging energy. At sizes above a_B^*, which is the relevant regime for lateral quantum dots, the charging energy is larger than the confinement energy. The crossover point between these two regimes is near a_B^*, which is $a_B^* \approx 10$ nm for GaAs. In the case that an empty orbital is filled, the charging energy and the orbital spacing together make up the addition energy $E_{add} = E_c + \Delta$, which is the energy required for the addition of a further electron to the dot. Due to orbital filling rules, sometimes only the charging energy needs to be paid in order to add an electron. Considering the Aufbau principle and Hund's rule for e.g. the case where each p-orbital in a p-shell is filled with one electron, the addition of another electron with opposite spin into one of the p-orbitals will only cost the charging energy [31,33].

Several experimental requirements need to be fulfilled in order to observe the Coulomb blockade in quantum dots. First, the tunneling resistance R_t from the quantum dot to the surrounding electron reservoirs, denoted as source and drain, needs to be sufficiently high. This can be shown by starting from the Heisenberg uncertainty relation $\Delta E \Delta t > h$ and considering the charging energy, i.e. $\Delta E = \frac{e^2}{C}$. For the time difference, the expression of the RC-time constant $\Delta t = R_t C$ can be considered. This leads to the condition

$$R_t > \frac{h}{e^2}, \tag{6}$$

and determines the minimum threshold for the tunneling resistance in order to observe Coulomb blockade. An additional implication of this uncertainty relation is that a weak tunnel coupling is better suited for the characterization of the Coulomb energy. Regarding the setup of the experiment, the electron temperature must be small compared to the relevant energy scales. This leads to the condition

$$k_B T \ll \frac{e^2}{C}, \tag{7}$$

meaning that the charging energy must be much larger than the electron temperature. If the condition

$$k_B T < \Delta \tag{8}$$

is fulfilled, the orbital spacing is visible in the measurements. Altogether, requirements (6)-(8) are needed in order to resolve the energy levels of a quantum dot. For the case of a quantum dot with $r \approx 15$ nm, inserting into eq. (3) and considering $\epsilon_{GaAs} = 13$ gives $E_c \approx 12$ meV (though, the charging energy will be smaller than this value due to screening effects by the surface gates and adjacent electron reservoirs), while for the estimate in eq. (5), a orbital spacing $\Delta \approx 1.3$ meV is obtained with $m^*_{GaAs} = 0.067 m_e$. Dividing these energies by the Boltzmann constant yields the conditions $T \ll 139$ K for (7) and $T < 15$ K for (8).

Qualitatively, the Coulomb blockade effect in a quantum dot can be explained with the schematic given in the inset of Fig. 2a, in which the quantum dot is tunnel coupled to the source and drain electron reservoirs and capacitively coupled to the surface gates. This treatment leads to the energy level diagram that is shown in Fig. 2c. Here, μ_S and μ_D denote the electrochemical potentials of the source and drain reservoirs. In the quantum dot, the electrochemical potential for the addition of the Nth electron is denoted as μ_N. By changing the plunger gate voltage by ΔV_p, μ_N is shifted by the amount $-|e|\alpha_p \Delta V_p$. In this expression, α_p is the lever arm of the plunger gate, a quantity that converts the change in gate voltage to a change in energy. From the above expression of the shift in μ_N, it is recognized that applying a more negative (positive) voltage increases (decreases) the electrochemical potential inside the dot.

In the case (I) shown in Fig. 2c, the electrochemical potentials of the source and drain are aligned. Starting with N electrons in the quantum dot, μ_N is situated below μ_S and μ_D while μ_{N+1} is above these levels. In this configuration, all available levels in the quantum dot are filled and no further transport occurs (disregarding thermal broadening of the leads). At such a configuration, the system is in Coulomb blockade. As the electrochemical potential in the dot is lowered using the plunger gate, there is a point where μ_{N+1} becomes resonant with μ_S and μ_D. In this configuration, electrons can, sequentially, tunnel elastically in and out of the dot, and a large peak in conductance is measured. As μ_{N+1} is tuned past this resonance point, the system re-enters Coulomb blockade. This transport behaviour leads to the characteristic, sharp conductance peaks at small bias.

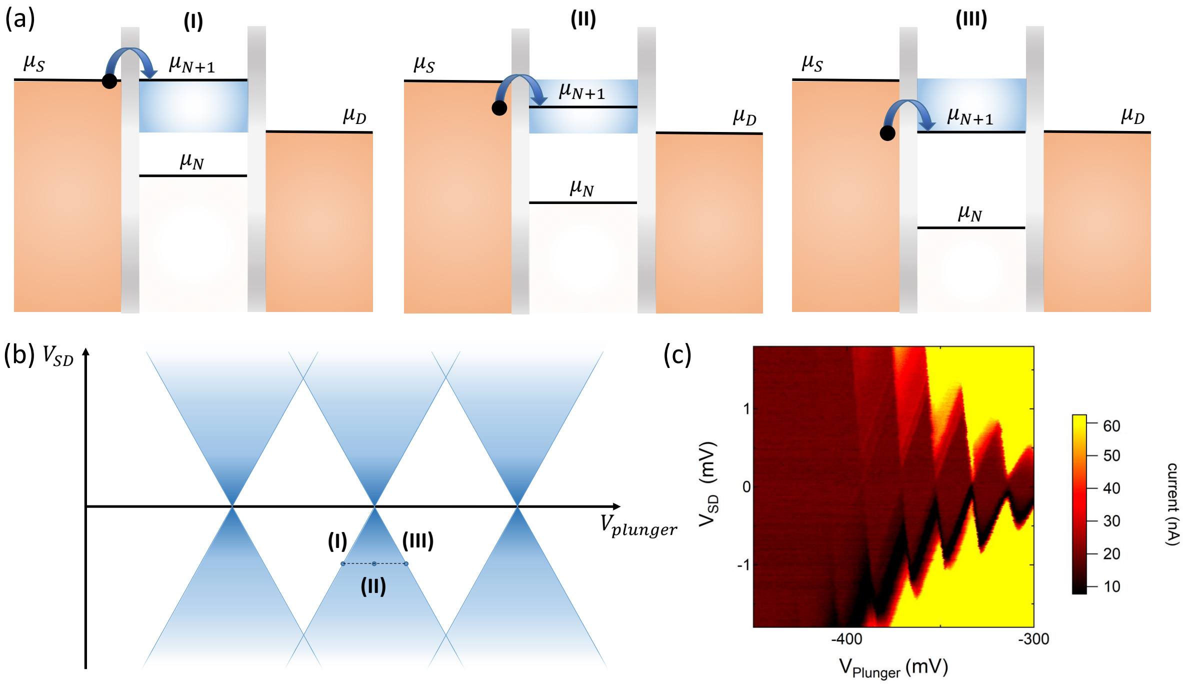

Figure 3: (a) Transport through the quantum dot in the case of a non-zero bias voltage V_{SD}, which changes the chemical potential in the source μ_S by $-|e|V_{SD}$ and opens a bias window (blue) between μ_S and μ_D. Transport through the dot is possible when the chemical potential corresponding to a quantum dot electronic state is within the bias window. (b) By scanning the bias voltage against the voltage on a plunger gate, the characteristic Coulomb diamonds that result from the opening of the bias window are obtained. The points (I)-(III) correspond to the three configurations in (a). (c) Measured Coulomb diamond plot, showing the bias voltage V_{SD} in dependence of the plunger gate voltage $V_{Plunger}$. Some excited states can be seen close to the edges of the diamonds.

When a non-zero bias voltage V_{SD} is applied between the source and drain reservoirs, the electrochemical potential of the source μ_S is changed by $-|e|V_{SD}$ and thereby opens the so-called bias window [16]. While at zero bias the transport could only occur in regions where μ_N was at resonance with the reservoir potentials, electron transport is now possible at any point where an energy level in the quantum dot is within the bias window. This is schematically depicted in Fig. 3a, showing three exemplary cases of transport within the transport window. When the bias voltage is scanned against the plunger gate, an increasing bias continuously opens the bias window. As a consequence, the plunger gate voltage region where Coulomb blockade occurs becomes increasingly narrow until it disappears. When such a measurement is performed for sufficiently negative and positive bias voltages, characteristic diamond-shaped regions of Coulomb blockade, called Coulomb diamonds, are obtained, as shown in Fig 3b and 3c. Such bias spectroscopy measurements can, for example, also serve as an useful instrument for the characterization of excited states inside the dot.

2.2.3 Charge sensing

Transport measurements through a quantum dot are limited by several factors. When the tunneling rates of the dot become too low, the current becomes too small to be directly measurable. Furthermore, the dot needs to be coupled to both reservoirs in order to observe transport. To bypass these issues, an additional quantum dot which is in close proximity of the investigated main quantum dot can be used as a charge sensor. In this approach, transport is measured through the sensor quantum dot instead of the main quantum dot. In principle, this allows for the non-invasive measurement of charge states in the main quantum dot, and also works if it is only coupled to one reservoir. With this measurement technique, real-time sensing of the charge state in the main quantum dot can be achieved. A time resolved charge sensing signal is shown in Fig. 4a for the single-electron regime, where the measured sensor conductance takes on two values, corresponding to the filled (high sensor conductance) and empty (low sensor conductance) state of the main quantum dot.

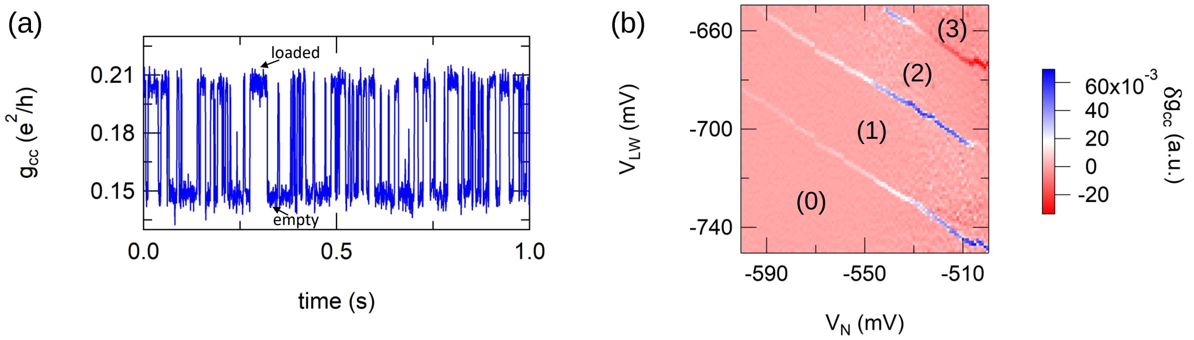

Figure 4: (a) Measured real-time charge sensing signal. When the sensor quantum dot is tuned to the falling edge of a Coulomb peak, the higher (lower) sensor conductance in this plot corresponds to a loaded (empty) quantum dot. (b) Differentiated signal of the measured sensor conductance δg_{cc} as a function of two center quantum dot gate voltages V_{LW} and V_N, belonging to the wall gate LW and the nose gate N in Fig. 2(a). At every configuration where tunneling processes occur, the sensor conductance rapidly changes, leading to a large amplitude in the differentiated signal. Brackets denote the number of electrons in the quantum dot. The experiments described in this thesis are carried out at the transition between the charge states (0) and (1).

In order to achieve a high sensitivity in the charge sensor, the sensor quantum dot is tuned to one of the flanks of a Coulomb peak. Due to the capacitive coupling to its electrostatic environment, the conductance in the sensor quantum dot changes whenever an electron tunnels on or off the main dot. In order to use this real-time technique, the time between tunneling events which is given by the tunneling rate needs to be shorter than the total measurement time. Furthermore, the bandwidth of the sensor needs to exceed the tunneling rate and the charge sensing signal needs to be larger than the noise.

As a consequence of the capacitive coupling, changes in gate voltages that are applied to the main quantum dot will cause the sensor quantum dot to be driven away from the operation point at the Coulomb peak flank, which negatively impacts the sensitivity of the charge sensor. To counteract this effect, a compensating voltage is applied to the plunger gate of the sensor quantum dot, thus serving as a feedback mechanism. Here, a linear compensation with a gate-specific correction coefficient is used. Though more refined compensation schemes are possible, a linear compensation is sufficient for the experiments in this thesis. Fig. 4b shows the charge sensing signal depending on the gates LW and N of the main quantum dot. A linear compensation to the sensor is applied for both gates, although the correction factor varies (i.e. it is larger for gates that are closer to the charge sensor). Such a plot is referred to as a charge stability diagram, as it shows regions of gate voltages where a certain number of electrons occupy the quantum dot. In the shown plot, the transition lines are close to diagonal at the same voltage difference, meaning that the quantum dot has a similar capacitive coupling to both gates.

2.3 Spin-orbit interaction

The spin-orbit interaction (SOI) is a relativistic effect that couples the orbital motion of a charge carrier with its spin degree of freedom. An electron that moves in an electric field $\vec{E}$ experiences in its resting frame a magnetic field

$$\vec{B'} \propto \vec{p} \times \vec{E}, \tag{9}$$

where $\vec{p}$ denotes the momentum and the dash denotes the resting frame of the electron. This magnetic field in turn couples to the spin degree of freedom of the electron, and the resulting dependency of the magnetic field on the orbital motion thus leads to the coupling of spin and orbit. For an electron that moves inside a GaAs 2DEG, there are two main electric field contributions that lead to spin-orbit interaction.

Dresselhaus SOI: The first electric field contribution stems from the zincblende crystal structure of GaAs. Because it belongs to the tetrahedral point group T_d, the zincblende crystal lacks an inversion center. This so-called bulk inversion asymmetry (BIA) causes an electric field, and the resulting contribution to the SOI is called Dresselhaus SOI [34]. For a 2DEG that is grown along the z-direction, the bulk Hamiltonian is considered where x, y and z correspond to the crystallographic directions [1 0 0], [0 1 0] and [0 0 1] respectively [35]. Considering the confinement in z-direction, the expectation value is given as $\langle p_z \rangle = 0$, leading to the reduced Dresselhaus Hamiltonian

$$\mathcal{H}_D^{2D} \propto [-p_x \langle p_z^2 \rangle \sigma_x + p_y \langle p_z^2 \rangle \sigma_y + p_x p_y^2 \sigma_x - p_y p_x^2 \sigma_y], \tag{10}$$

where p_i are the components of the momentum vector $\vec{p}$ and σ_i are the components of the Pauli spin vector $\vec{\sigma}$. This reduced Hamiltonian consists of two terms that are linear and two terms that are cubic in momentum. For a narrow 2DEG and thus strong confinement in z-direction, the cubic terms are usually neglected because $\langle p_z^2 \rangle \gg p_x^2, p_y^2$ [16], and the material-specific Dresselhaus coefficient β_D can be introduced, leading to

$$\mathcal{H}_D^{2D} = \beta_D [-p_x \sigma_x + p_y \sigma_y]. \tag{11}$$

Rashba SOI: The second contribution to the electric field arises from the confining potential of the heterostructure which hosts the 2DEG. Here, the structural inversion asymmetry (SIA) of the triangular quantum well creates an electric field in the GaAs side of the heterojunction. This contribution is called Rashba SOI [36, 37]. When only the electric field caused by the confining potential is considered, i.e. $\vec{E} = (0, 0, E_z)$, this results in a Hamiltonian of the form

$$\mathcal{H}_R \propto [\vec{E} \times \vec{p}] \vec{\sigma} = E_z [-p_y \sigma_x + p_x \sigma_y], \tag{12}$$

which can also be written as

$$\mathcal{H}_R = \frac{\alpha_R(z)}{\hbar} [-p_y \sigma_x + p_x \sigma_y]. \tag{13}$$

In this expression, α_R denotes the material-specific Rashba coefficient [16]. This prefactor can be approximated as

$$\alpha_R(z) = \alpha_0 e E_{ext} + \beta_{BA} \delta(z), \tag{14}$$

where the interface electric field $E_{ext} = \frac{\hbar^2}{2 m l_z^3 e}$ can be calculated from the 2DEG width l_z [12, 38]. Furthermore, α_0 and β_{BA} are material constants which are given in Ref. [39]. In expression (13), the term

$\alpha_0 e E_{ext}$ is understood as the slope in the confining potential while the term $\beta_{BA}\delta(z)$ stems from the sudden jump due to the band gap offset of GaAs and AlGaAs.

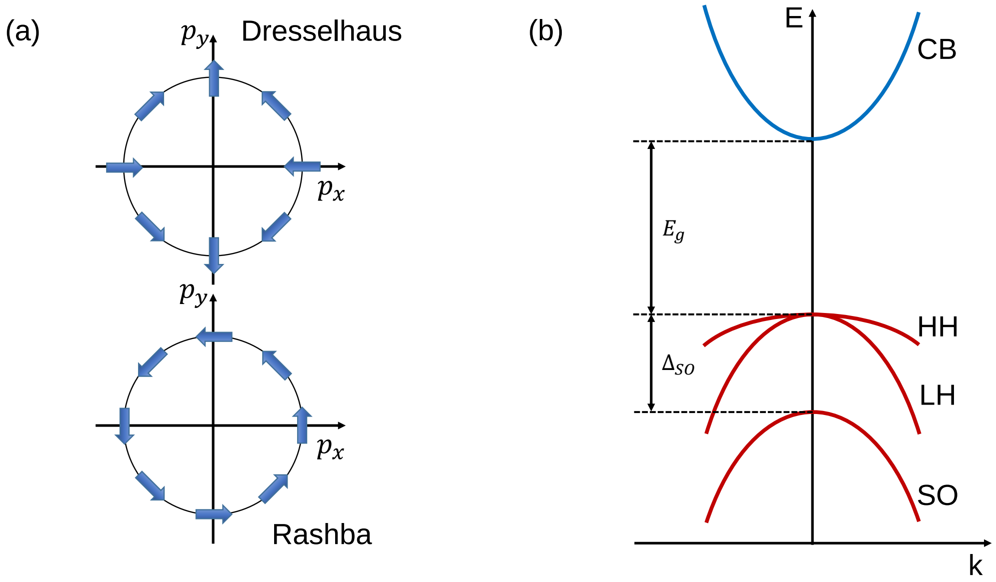

Figure 5: (a) Diagram for the directionality of the internal magnetic field that an electron with momentum $\vec{p}$ experiences due to the Dresselhaus SOI and the Rashba SOI, drawn as blue arrows in the $p_x p_y$-plane. (b) Band structure diagram in the effective mass approximation, shown around k=0. The conduction band (CB) is separated from the heavy-hole (HH) and light-hole (LH) valence bands by the band gap energy E_g. The upper HH and LH valence bands are separated from the split-off (SO) band by the spin-orbit splitting Δ_{SO}.

From the Hamiltonians given in Eq. (11) and Eq. (13), it is seen that the Dresselhaus SOI and the Rashba SOI differ in their dependence on the direction of the electron momentum $\vec{p}$. For the Dresselhaus SOI, the effective magnetic field is aligned with the momentum in the y-direction while it is opposite to the momentum in the x-direction. On the other hand, the effective magnetic field for the Rashba SOI is orthogonal to the momentum for any direction. This is shown in Fig. 5a, where the magnetic field direction that the moving electron experiences is shown in dependence of the momentum direction.

Band structure effects: In order to show the influence of spin-orbit effects on a quantity such as the g-factor, the typical semiconductor band structure needs to be considered. Here, the region of interest lies in the fundamental band gap that is schematically depicted in Fig. 5b as an effective mass approximation around the Γ point at k=0. In this diagram, the lowest conduction band (CB) and the three uppermost valence bands are shown. The conduction band is separated from the two upper valence bands (which are called the heavy-hole (HH) and the light-hole (LH) band, stemming from the difference in their effective mass m^*) by the band gap energy E_g. The last of the three valence bands is referred to as the spin-orbit split-off band (SB) and is separated from the others by the spin-orbit splitting Δ_{SO}. States in the conduction band are s-like with an angular momentum quantum number $L = 0$, whereas the states in the valence bands are p-like with $L = 1$. Considering only the simple picture where the experienced magnetic field is proportional to the momentum, one would therefore expect weaker SOI effects to occur for electrons in the lowest conduction band than for holes in the valence bands. However, a thorough analysis within the **k** · **p** theory framework [35] reveals that for electron and hole states alike, higher-order coupling processes with the neighbouring bands lead to spin-orbit interaction effects that are on the same order of magnitude. The extent to which the SOI affects the states in the conduction band is determined by both the spin-orbit splitting Δ_{SO} and the band gap energy E_g. This interplay of energies is for example reflected in Roth's formula [40], which approximates the effective g-factor in semiconductors as

$$\frac{g^*}{2} = \frac{g'}{2} - \frac{2m_0}{\hbar^2}\frac{P^2}{3}\left(\frac{1}{E_g} - \frac{1}{E_g + \Delta_{SO}}\right). \tag{15}$$

In this expression, P denotes the matrix element for the coupling between the conduction and valence bands, g' the g-factor without considering the coupling effects and g^* the effective g-factor. Comparing for example the materials GaAs ($\Delta_{SO} \approx 0.34$ eV, $E_g \approx 1.5$ eV, $g^* = -0.44$) and InAs ($\Delta_{SO} \approx 0.38$ eV, $E_g \approx 0.42$ eV, $g^* = -14.9$) [35], GaAs has a similar spin-orbit splitting, but the much smaller band gap energy of InAs leads to a far more negative effective g-factor and in general, electrons in InAs experience a much stronger SOI.

2.4 Corrections to the g-factor

This section briefly summarizes the theoretical model and findings that are outlined in full detail in Ref. [12]. These are follow-up calculations to the theoretical approach of Ref. [39], where the orbital effects of an in-plane magnetic field on a 2DEG were investigated.[1] The motivation here was that for strong magnetic fields, the magnetic length $l_B = \sqrt{\frac{\hbar}{eB}}$ becomes comparable to the width of the 2DEG, thus making the treatment as a quasi two-dimensional system inaccurate. Using a perturbative approach based on the **k** · **p** theory and the envelope function approximation [35], corrections to the excited orbital state energies could be predicted and measured in experiment [32]. With the knowledge over these orbital corrections, a new spectroscopy method that allows for the determination of the shape, size and orientation of a quantum dot in such a device was established.

By also including the spin-dependent terms that arise from the aforementioned orbital effects, Stano et al. predicted corrections to the g-factor that originate from a variety of spin-orbit terms. Namely, these terms are not time reversal symmetric because they are generated by the magnetic field, and therefore contribute to a correction of the g-factor in the lowest order. The calculations are based on the Ogg-McCombe Hamiltonian [41,42], which contains terms that are allowed for the tetrahedral point group T_d and the relevant conduction band Γ_6, going up to the fourth order in momentum and using band structure coefficients from Ref. [43]. For the calculations, the quantum dot shape was chosen to be nearly circularly symmetric in the 2DEG plane. The g-factor corrections that were obtained from this perturbation theory are shown in Fig. 6, depending on the 2DEG width (a) and the magnetic field (b). In Fig. 6a, solid (dashed) lines correspond to an in-plane magnetic field $B = 0$ T ($B = 6$ T) whereas in Fig. 6b, solid (dashed) lines correspond to a 2DEG width of approximately 6.4 nm (10.4 nm).

In these plots, g_r (g_d) stems from higher-order contributions of the Rashba (Dresselhaus) SOI, whereas the terms g_{43}, g_{44}, g_{45} originate from terms in the Ogg-McCombe Hamiltonian and g_{47} comes from an additional term that was taken from Ref. [35]. The correction g_p is caused by the penetration of the wave function into the neighbouring AlGaAs material, thus causing a deviation from the g-factor of bulk GaAs when the 2DEG becomes too narrow, which is a well researched effect [44,45]. Furthermore, this

---

[1] Considering for example the application as a spin qubit, out-of-plane magnetic fields are avoided as they lead to strong orbital effects due to the Lorentz force.

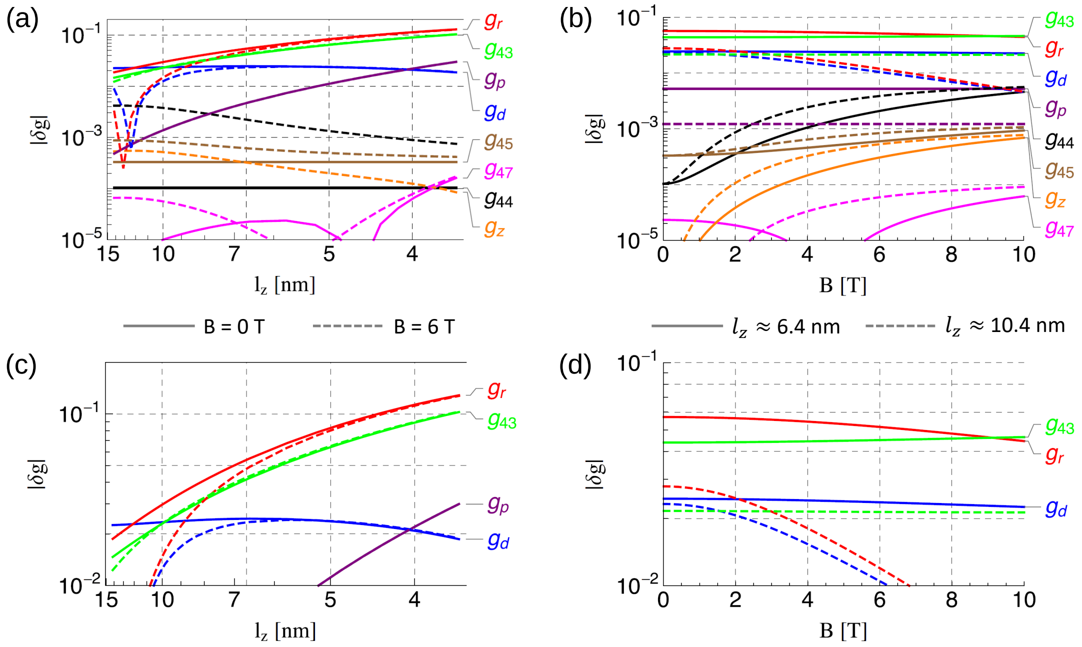

Figure 6: Predicted absolute corrections to the g-factor $|\delta g|$ from Ref. [12], shown in dependence of the 2DEG width l_z (left graphs) and the magnetic field B (right graphs). These calculations assume the quantum dot in the ground state and lowest subband, with orbital energies $E_x = 2.34$ meV and $E_y = 2.61$ meV, corresponding to lengths $l_x \approx 22$ nm and $l_y \approx 21$ nm. The quantum dot was assumed to be rotated from the crystal axis [1 0 0] by an angle $\delta = 25°$ and the angle of the magnetic field relative to [1 0 0] was set as $\phi = 45°$. (a) g-factor corrections for a fixed magnetic field and a 2DEG width ranging from 15 nm to below 4 nm. Solid lines denote the corrections at zero in-plane magnetic field while dashed lines correspond to the case B = 6 T. (b) g-factor corrections for a fixed 2DEG width and a varying magnetic field, ranging from 0 T to 10 T. Solid (dashed) lines correspond to a 2DEG width of approximately 6.4 nm (10.4 nm). (c) Same plot as in (a), but showing only the strongest correction values between 10^{-1} and 10^{-2}. This reduces the set of correction terms to four terms, which originate from the Rashba SOI (g_r), the Dresselhaus SOI (g_d), one of the SOI contributions from the Ogg-McCombe Hamiltonian (g_{43}) and the wave function penetration (g_p), which falls below 10^{-2} for a 2DEG width over 5 nm. (d) g-factor corrections from (b) shown in the range from 10^{-1} to 10^{-2}. Only the terms g_{43}, g_r and g_d lead to sizable corrections for the two considered 2DEG widths. All figures are adapted from Ref. [12].

correction does not depend on the strength of the magnetic field. There is also a correction g_z, which is caused by the inhomogeneous g-factor in the bulk material. The corrections go up to the third order in magnetic field, but none of them show linear dependence on the magnetic field.

Focusing on the most significant corrections above the magnitude of 10^{-2}, there are four terms that remain and are depicted in dependence of the 2DEG width l_z in Fig. 6c. Considering $l_z \approx 6.4$ nm as determined in [32], the Rashba SOI contribution g_r and a generic SOI contribution g_{43} are the strongest corrections. The correction from the Dresselhaus SOI is the third strongest, whereas the contribution from the penetration of the wave function is below 10^{-2} for this 2DEG width. This can also be seen in Fig. 6d, where g_p is absent. In general, these g-factor corrections become weaker with an increasing l_z. For $l_z \approx 6.4$ nm, the corrections g_{43} and g_d are close to constant in magnetic field, whereas g_r slightly decreases by approximately 10^{-2} over the range of 10 T.

Additionally, the directionality of the different g-factor corrections was considered. Looking at the three strongest correction terms, g_r and g_{43} are isotropic in the plane of the 2DEG whereas g_d is

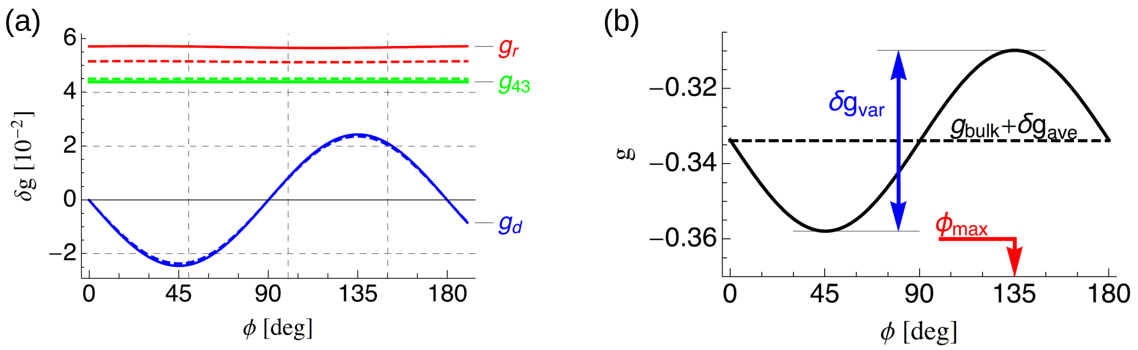

Figure 7: (a) Dependence of the g-factor corrections on the magnetic field direction, here shown with the angle ϕ for zero in-plane field (solid curves) and an in-plane field of 6 T (dashed curves). Further parameters are the same as for the graphs in Fig. 6. Although the terms g_r and g_{43} dominate the g-factor corrections, they don't change with the direction of the in-plane field, thus constituting the isotropic part of the corrections. The term g_d is anisotropic with regards to the in-plane field directions and dominates the anisotropic contribution to the g-factor. (b) Predicted dependence of the overall g-factor on the direction of the in-plane magnetic field. The g-factor averages at a value around -0.33 and shows an anisotropic correction δg_{var} with a variation around ±7%. The maximum of the g-factor is reached at $\phi_{max} = 135°$. The figures are adapted from Ref. [12].

anisotropic. This is shown in Fig. 7a, where the most relevant g-factor corrections (for $l_z \approx 6.4$ nm) are plotted against ϕ, denoting the angle relative to the crystal axis [1 0 0]. Interestingly, and unlike for a 2DEG of larger width, the g-factor anisotropy is independent of the magnetic field. Using data from the experiments in [14] and [32], Stano et al. predicted an average g-factor around -0.33 that varies by about ±7% depending on the angle ϕ, as shown in Fig. 7b.

3 Materials and Methods

The measurements that are presented in this thesis were carried out on a spin qubit device based on the GaAs/AlGaAs heterostructure shown in Fig. 1a. The wafer was grown by the Gossard group at UCSB. It has a Si δ-doping concentration of $n_\delta = 4 \cdot 10^{12}$ cm^{-2}, a mobility $\mu = 2.8 \cdot 10^5 \frac{cm^2}{Vs}$ and a 2DEG density $n = 2.8 \cdot 10^{11}$ cm^{-2}. The depletion gates on top of the device are nominally the same as the ones shown in the scanning electron micrograph in Fig. 2a. Negative voltages are applied to the gates, leading to the formation of a quantum dot in the center of the device. Furthermore, a second quantum dot is formed on the right side of the device, adjacent to the right wall gate RW, serving as a charge sensor. The main quantum dot is tuned to the last electron regime. Furthermore, the sensor configuration is optimized such that real-time tunneling events can be observed.

The gate CP is used as a pulsing gate by adding an AC pulse signal to its DC component. The pulses are applied using a National Instruments USB-6366 DAQ device with a pulsing (readout) bandwidth of 3.3 MHz (2 MHz). The measurements are carried out in a dilution refrigerator (MCK 76 TOF Dilution refrigerator, Leiden Cryogenics) with an electron temperature of 210 mK (see Sec. 4.1).[2] Voltages are applied on the gates and Ohmic contacts of the device using a low noise high resolution digital-to-analog converter (LNHR DAC, Basel Precision Instruments). The current through the sensor quantum dot is measured using a low noise high stability I/V converter (LNHS I/V converter, Basel Precision Instruments) and read out with the DAQ. Lines that connect to the experiment show a resistance of approximately 40 Ω and have microwave filters with a capacitance of 5 nF [46]. To reduce capacitance-induced noise, some of the lines (namely, one line for an Ohmic contact at each of the two possible sensor quantum dot sites) have microwave filters with a reduced capacitance of 2 nF. Though, for the experiment described in this thesis none of the Ohmic contacts on the chip were disconnected. Thus, the two Ohmic contact lines at the I/V converter are in parallel, leading to $R_{tot} = 20\ \Omega$ and $C_{tot} = 7$ nF. This leads to a technical bandwidth of approximately 1 MHz.[3] The low pass filter on the I/V converter was set to 3 kHz and a gain factor of 10^7 was chosen.[4]

In order to apply an in-plane magnetic field, a superconducting solenoid (14/16T magnet, Cryogenics Ltd) surrounds the fridge insert at the height of the chip holder. In our setup, this magnet can reach a field strength of up to 14 T. The sample can be rotated with a piezo rotator (Attocube ANRv51) around the axis perpendicular to the chip, thus making it possible to change the direction of the in-plane magnetic field. By doing a Van der Pauw measurement (see Appendix A.1), the out-of-plane angle of the magnetic field was determined to be smaller than 1.5° and thus assumed to be negligibly small for the purpose of this experiment.

3.1 Measurement of the tunneling rate

As a starting point for the determination of the tunneling rate, the quantum dot level of the last electron transition is tuned to the chemical potential μ_S of the reservoir, leading to a real-time charge sensing signal such as the one shown in Fig. 4. The more thorough treatment of the following calculations can be found in Ref. [47]. Here, the charge sensing signal (see Sec. 2.2.3) is regarded as a two-level system being either in the "on" (high conductance) or "off" (low conductance) state. A threshold is chosen

---

[2] For the experiment presented in this thesis, a different plastic dilution unit than in the first device of Ref. [1] was used. Here, the heat exchangers were less efficient, which prevented cooling below 100 mK.

[3] The technical bandwidth was calculated using $f_c = \frac{1}{2\pi RC}$ for an RC circuit.

[4] A higher cutoff frequency of 10 kHz or 30 kHz on the I/V converter caused problems with the noise - in our setup, the higher harmonics of the 50 Hz noise were amplified at high magnetic fields due to coupling of vibrations at the refrigerator gas handling system with the magnet, leading to Eddy currents.

exactly halfway between the maximal and the minimal signal in order to distinguish the two levels. For a quantum dot, it can be shown that the distribution of time intervals t_{on} (t_{off}) that an electron resides on (off) the dot has an exponential dependence on the tunneling rate (off) on the dot, i.e.

$$\rho_{on}(t_{on}) \propto exp(-\Gamma_{off} t_{on}), \qquad \rho_{off}(t_{off}) \propto exp(-\Gamma_{on} t_{off}), \tag{16}$$

where Γ_{on} (Γ_{off}) is the tunneling rate on (off) the quantum dot [47]. This means that a high Γ_{on} (Γ_{off}) decreases the time intervals where the quantum dot is in the "off" ("on") state. Thus, the tunneling rates can be obtained from fitting an exponential function through histograms of t_{on} and t_{off}.[5] Furthermore, the probability P_{on} for the electron to reside on the quantum dot can be expressed as a function of the tunneling rates by

$$P_{on} = \frac{1}{1 + \frac{\Gamma_{off}}{\Gamma_{on}}}, \tag{17}$$

and $P_{off} = 1 - P_{on}$. The term in the denominator can also be written as

$$\frac{\Gamma_{off}}{\Gamma_{on}} = \frac{1}{2} exp(\frac{-e\alpha_g V_g}{k_B T_e}), \tag{18}$$

where e is the elementary charge, α_g the lever arm of the gate, V_g the gate voltage, k_B the Boltzmann constant and T_e the electron temperature. From Eq. (17) and (18) it becomes clear that the electron transition follows a Fermi-Dirac distribution. Thus, the calculated tunneling rates are an useful instrument for the extraction of the electron temperature. Also, in combination with a varying temperature at the device, such probing of the transition can be used in order to determine the lever arm of a given surface gate (see Sec. 4.1). An exemplary tunneling rate measurement along a transition is shown in Fig. 8, where the rates Γ_{on} and Γ_{off} are shown in combination with the occupation probability P_{on}. At the point where $\Gamma_{on} \approx \Gamma_{off}$, the chemical potential μ is aligned with the ground state level in the quantum dot, thus allowing electrons to tunnel in and out of the dot with the same intermediate rate Γ_{int}.

3.2 Drift compensation algorithm

Prior to measurements, the quantum dot is tuned to a region of the last electron transition such as in Fig. 4b, and the charge sensor is adjusted in order to maximize the signal-to-noise ratio. Before describing the applied pulsing schemes in further detail, the stability of the quantum dot needs to be considered. Especially when data are taken over hundreds of measurement rounds for proper statistics, the electron transition needs to be traced over a time frame that can be upwards of 10 hours. At such long times, random charge fluctuations in the wafer material will cause drifts in both the investigated transition and in the charge sensor operating point. Therefore, the measurement protocols need to be able to compensate for such drift processes. Here, this is done through the implementation of a drift compensation algorithm that is usually applied before every measurement round. The algorithm changes one of the gate voltages such that a certain fixed tunneling rate onto the quantum dot is obtained - this is the set point for the drift correction.[6] In its first step, the algorithm measures the rates Γ_{on} and Γ_{off} as explained in Sec 3.1. In order to calculate the incremental changes in voltage that are needed to reach the

---

[5] Here, the time intervals are plotted on a logarithmic scale and a line is fitted through, making the automatic fitting process easier.

[6] Different set points are chosen for the protocols described in this section. For the excited states spectroscopy, the drift compensation tries to reach the point where $\Gamma_{on} = \Gamma_{off}$. In the tunneling rate measurements for the g-factor, a reference point $\Gamma_{on} = 20$ Hz with a tolerance threshold $\Gamma_{tol} = 3$ Hz was used.

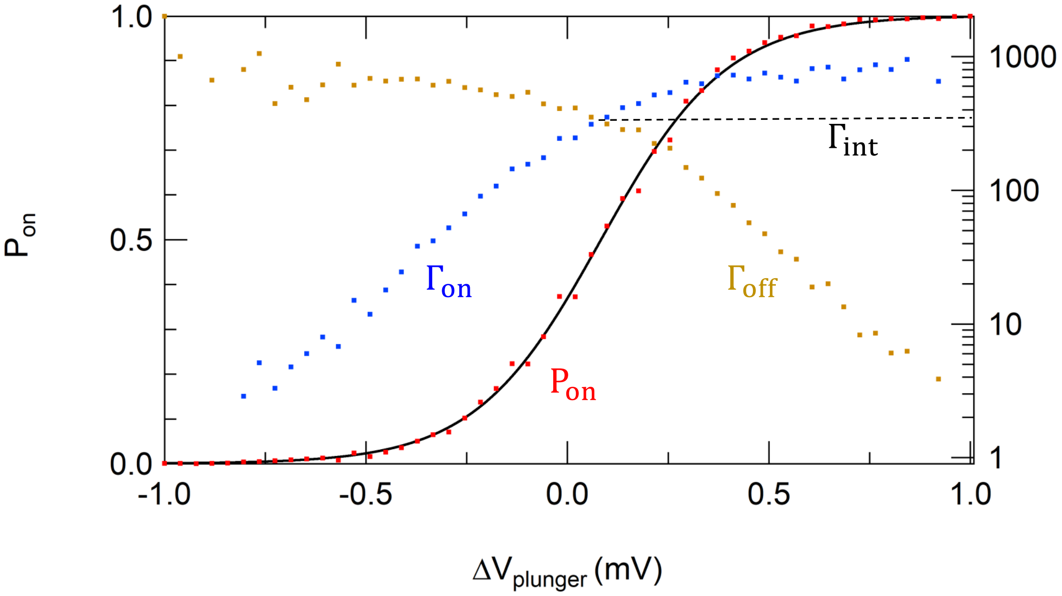

Figure 8: Occupation probability P_{on} (red dots), Γ_{on} (blue dots) and Γ_{off} (orange dots) in dependence of the plunger gate voltage $V_{plunger}$. A Fermi-Dirac distribution is fitted through P_{on} (solid line). Here, an intermediate tunneling rate $\Gamma_{int} = 312.7$ Hz was measured.

set point, the transition is assumed to be at the exponential tail of the Fermi-Dirac distribution such that $\Gamma_{on} \propto e^{\frac{e\alpha V_g}{k_B T_e}}$. The logarithmic value of Γ_{on} along the transition is then used for the implementation of a linear compensation. If $\Gamma_{on} > \Gamma_{set}$, the gate voltage will be made more negative for the next iteration, and a less negative gate voltage will be applied if $\Gamma_{on} < \Gamma_{set}$. For a tunneling rate at the chemical potential of about 100 Hz, a measurement time t_{meas} of about 10 s is chosen. The feedback loop continues until it measures a rate Γ_{on} within a window close to Γ_{set}, defined by the tolerance threshold Γ_{tol}. If this is the case, the drift compensation algorithm has succeeded and the measurement can begin.

3.3 Measurement of the lever arm

The lever arm of a given gate is an important quantity for the conversion of a change in gate voltage to a change in energy. When the quantum dot is tuned closer to a gate, the lever arm of that gate increases, i.e. a change in applied voltage leads to a larger change in energy. In Ref. [28] it was shown that for a large set of dot geometries (spanning gate voltage differences of hundreds of mV), the lever arm of the plunger gate remains fairly similar. In order to keep this assumption also valid for the experiments in this thesis, an effort was made to keep the gate voltages close to a standard configuration for all measurement points.[7] Furthermore, in Ref. [28] it was also found that the lever arm does not depend on the magnetic field for the range of fields that is used in the experiment. Thus, the lever arm measurement that is explained here was only done for the standard gate configuration at zero magnetic field.

To measure the lever arm of the relevant central plunger gate, the quantum dot was tuned to the last electron at an increased tunneling rate of approximately 300 Hz, such that a decreased measurement time t_{meas} (see Sec. 3.2) of 5 s could be chosen. Furthermore, the temperature at the sample was increased to

---

[7] More exactly, only the gate voltages on CP, LW, N and SEP (left) were varied by at most 150 mV throughout the measurements. This was done to bypass measurement artefacts from the reservoir and the decreasing tunneling rate at high magnetic fields.

a few hundred mK by applying a current to a heater in the mixing chamber. The reason for this is that at base temperatures of a dilution refrigerator, it has been shown that the electron temperature T_e exceeds the temperature in the mixing chamber [28, 48]. Furthermore, the temperature-induced broadening of the transition also reduces the uncertainty in the extracted lever arm. For the lever arm measurement presented in this thesis, the coldfinger temperature T_{CF} (RuO_2 R-2Kxcmn-5coeff thermometer, read out with a Picowatt AVS-47) was increased from its standard operating point of 150 mK up to an increased temperature of 700 mK, where T_e and T_{CF} are assumed to be the same. Using the method presented in Sec. 3.1, 4 to 10 measurements of T_e were made for each value of T_{CF}.

3.4 Measurement of the g-factor

In this thesis, the g-factor is determined through pulse-gate spectroscopy of the tunneling rate into the empty quantum dot. This is done at the (0) ↔ (1) transition in Fig. 4b in dependence of the detuning ΔE from the pulsed plunger gate. In presence of an external magnetic field, spin degeneracy of the ground state is lifted. In GaAs, this causes the spin state $|\uparrow\rangle$ to become lower in energy than $|\downarrow\rangle$ by the Zeeman splitting $\Delta E_Z = g\mu_B B$.[8] The tunneling rate $\Gamma(\Delta E)$ close to the Zeeman split transitions is qualitatively explained by the expression

$$\begin{aligned}\Gamma(\Delta E) &= \Gamma_\uparrow(\Delta E) + \Gamma_\downarrow(\Delta E)\\ &= \Gamma_0 e^{-\beta\Delta E}\Big[f(\Delta E, k_B T) + \chi f(\Delta E + \Delta E_Z, k_B T)\Big].\end{aligned} \tag{19}$$

Eq. (19) describes the tunneling rate as a sum of tunneling rates into the $|\uparrow\rangle$ state ($\Gamma_\uparrow$) and into the $|\downarrow\rangle$ state ($\Gamma_\downarrow$). In principle, the tunneling rate into these two states only increases when they are aligned with the chemical potential μ of the reservoir. However, the states in the reservoir are occupied with a Fermi-Dirac distribution, i.e.

$$f(\Delta E, k_B T) = \frac{1}{(e^{\frac{\Delta E}{k_B T}} + 1)}, \tag{20}$$

which means that the two resonance conditions $\Delta E = 0$ (for $|\uparrow\rangle$) and $\Delta E = \Delta E_Z$ (for $|\downarrow\rangle$) in Eq. (19) are thermally broadened. The prefactor originates from the WKB approximation, which describes the tunneling rate Γ through a square tunnel barrier of height V_0 and length l as

$$\Gamma \propto \Gamma_{WKB} \cdot e^{-\sqrt{\beta_{WKB}(V_0 - E))}}. \tag{21}$$

Here, Γ_{WKB} is a scaling parameter and $\beta_{WKB} = 8m^* l^2/\hbar^2$ depends on the length of the tunnel barrier. The square root in the WKB approximation can be linearized for small detunings, leading to the dependence $\Gamma(\Delta E) \propto \Gamma_0 e^{-\beta\Delta E}$ as used here [49], where Γ_0 and β depend on the properties of the tunnel barrier. This WKB prefactor also explains the exponential decay of the tunneling rate when the dot levels are pulsed beyond the point of resonance (see Fig. 9d and Fig. 10b), which is a result of the increasing tunnel barrier.

Finally, in Eq. (19) there is a factor χ in front of the Fermi-Dirac distribution belonging to the $|\uparrow\rangle$ state. This factor gives the ratio between tunneling rates as $\chi = \Gamma_\downarrow/\Gamma\uparrow$ and thus describes a spin tunneling asymmetry. Previous experiments in GaAs quantum dots have shown that the spin tunneling asymmetry can vary from $\chi \approx 1$ down to $\chi \ll 1$, decreasing with the strength of the in-plane magnetic field [50]. This effect is unexpected because even though the spin states in the quantum dot differ in

---

[8] The g-factor in GaAs is negative - as opposed to the case of a free electron with positive g-factor, the spin ground state is thus $|\uparrow\rangle$ which is anti-aligned to the external field.

energy by the Zeeman splitting ΔE_Z, the conduction band is also subjected to Zeeman splitting and thus should experience the same tunnel barriers. A conclusive theoretical explanation for this spin tunneling asymmetry has not been found yet (the theoretical predictions for differences in χ due to a g-factor difference between reservoir and dot are far smaller than in experiments), though it is suspected that the effect mainly occurs because the g-factor in the reservoir is anomalously enhanced when it is subjected to a lateral confinement [51,52].

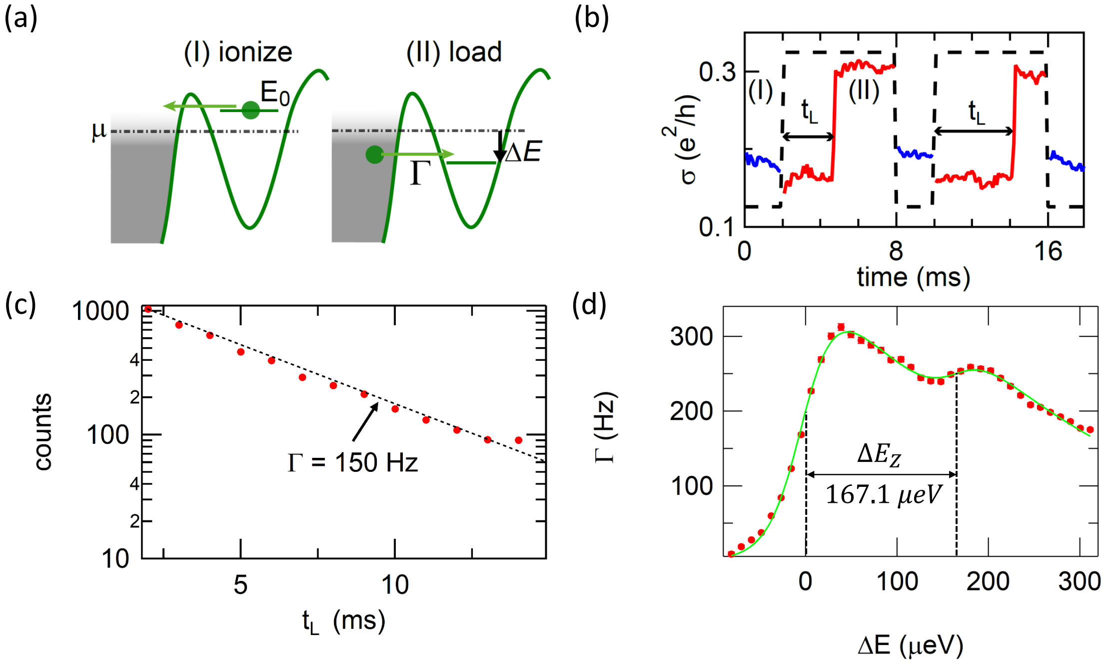

Figure 9: (a) Working principle of the pulse scheme for the g-factor measurement. The quantum dot is first ionized by pulsing the ground state E_0 above the chemical potential (I). Then, it is pulsed below the chemical potential μ with an amplitude of ΔE, resulting in the dot being loaded with an electron (II). (b) Overlay of an exemplary pulse (dashed) and the measured charge sensor conductance (solid). The charge sensor conductance during pulse step (I) is shown in blue, whereas the signal during (II) is colored red. When the previously ionized dot is pulsed to (II), it takes a loading time t_L until the dot is occupied with an electron. Figures (a) and (b) are adapted from Ref. [1]. (c) By fitting a line through the log-scaled histograms of t_L, the tunneling rate Γ for a point ΔE is obtained. (d) Exemplary data of a g-factor measurement, showing the tunneling rate in dependence of the detuning ΔE. The Zeeman splitting ΔE_Z is the energy between the two spin states by fitting Eq. (19), shown in green.

Pulse scheme: Prior to the g-factor measurement, the quantum dot is tuned to the transition of the last electron at an intermediate tunneling rate of approximately 100 Hz, which is determined with the method in Sec. 3.1. To measure the tunneling rates of the Zeeman split spin states, a two-step square voltage pulse is applied to the central plunger gate (CP in Fig. 2a). The two steps of the pulse correspond to the configurations that are shown in Fig. 9a: First, the states in the quantum dot are pulsed above the chemical potential of the reservoir, which causes any electron in the quantum dot to quickly tunnel into the reservoir. This ionization occurs much faster than the bandwidth of the charge sensor. Then, the states are pulsed below the chemical potential. At this configuration, an electron will tunnel into the dot after a loading time t_L given by Γ_{on}, which is observed in the charge sensor signal as shown in Fig. 9b. To keep the charge sensor at its sensitive operation point, a weaker compensation pulse of opposite sign is simultaneously applied to the sensor plunger gate. By repeating this scheme for up to 20'000 cycles, it is then possible to extract tunneling rates by fitting histograms of t_L as shown in Fig. 9c.

This measurement protocol is carried out for 100 to 400 rounds in total, where each of the rounds works as follows: First, the drift compensation algorithm (see Sec. 3.2) is applied using a set point of 20 Hz which corresponds to $\Delta E = 0$. After the algorithm has converged, the pulse scheme described above is used for different values of ΔE across the transition, using pulse times of 2 ms at the ionization step and 30 ms at the loading step. In order to avoid hysteresis effects, the sequence of detuning values is chosen randomly. In presence of a magnetic field, such a measurement allows for the extraction of the Zeeman splitting ΔE_Z by fitting the data and determining the energy difference between the Fermi edges corresponding to the two spin states. Here, fits are either made with Eq. 19 itself or an adjusted version of it with different factors β for the two spin states. In the case that fitting with these functions does not succeed, owing to resonance artefacts or suppressed tunneling into the excited spin state (see Sec. 4.3), a sigmoid function is fitted to the two spin transitions. These fit procedures yield very comparable Zeeman energies, which is the quantity of interest for this work.

3.5 Measurement of excited orbital states

In lateral GaAs quantum dots, the shape can be changed with the surface gate voltages (see Sec. 2.2.1). For example, the dot shape has been shown to have an effect on the spin-relaxation time T_1 due to the mixing of the orbital and spin states [53]. As it has been outlined in theory [39] and experiment [32], probing of the excited orbital states in a magnetic field gives insight on the shape of the quantum dot: Under assumption of a harmonic dot confinement, the energy E_x of the first excited orbital state that is oriented along $\hat{x} = [\bar{1}\,\bar{1}\,0]$ will increase when the dot is squeezed along this direction, and the same happens for the E_y orbital state when it is squeezed along the $\hat{y} = [1\,\bar{1}\,0]$ direction. These orbital energies are on the order of a few meV for usual experimental parameters, and a change in shape is compensated with gates perpendicular to the squeezing direction in order to keep the ground state energy constant. Considering for example a dot that is squeezed in $\hat{x}$ and elongated in $\hat{y}$, it follows from the above made considerations that the energy E_x will be higher than E_y. This tuning of the shape can be done continuously, ranging from a dot that is squeezed in $\hat{x}$ with $E_x > E_y$ to a dot that is squeezed in $\hat{y}$ with $E_y > E_x$. At the crossover point where $E_x \approx E_y$, the dot is symmetric [32, 50].

Whether an excited orbital state is E_x or E_y can be identified by applying an in-plane magnetic field: If the directions of the magnetic field and the orbital state are the same, its energy will remain constant with increasing field strength while the energy of the orthogonal orbital will decrease [39]. For example, an increasing magnetic field along the $\hat{x}$ direction will leave E_x unchanged and decrease E_y. Therefore, this spectroscopy technique allows to fully describe the orientation of the orbitals. From the behaviour of the state which is not constant in magnetic field, the energy E_z can be obtained, thus allowing to fully determine the three-dimensional shape of the quantum dot.

Pulse scheme: As for the g-factor measurements, the pulsing for the characterization of excited orbital states is done with the central plunger gate CP. Prior to the protocol, the tunneling rate into the ground state is tuned to a value between 10 and 100 Hz. The idea of the pulse scheme is illustrated in Fig. 10a. Here, the pulse sequence consists of three steps. The dot is initialized (I) by pulsing the ground state above the chemical potential of the reservoir μ, leading to its fast ionization as the electron tunnels out of the dot. Next, the dot is charged (II) by pulsing the quantum dot below μ by an amplitude ΔV_p (for a short time compared to the tunneling rate into the ground state). When an excited orbital state

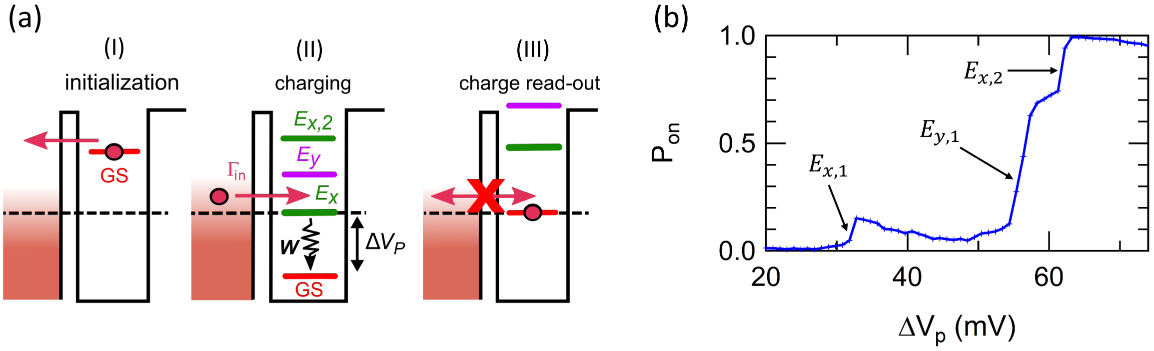

Figure 10: (a) Working principle of the pulse scheme for the measurement of excited orbital states. The quantum dot is first initialized (I) by pulsing the ground state above the chemical potential μ of the reservoir. Then, it is charged (II) by pulsing at an amplitude ΔV_p for a time t_w. When an excited orbital state is brought into resonance with μ, it tunnels in with a rate Γ_{in} and then decays to the groundstate at a relaxation rate W. Finally, charge readout (III) is carried out by pulsing the ground state into resonance with μ for 500 μs, which allows to extract the occupation probability P_{on} at a given ΔV_p. Adapted from Ref. [28]. (b) Exemplary data of an excited orbital state measurement, showing P_{on} in dependence of ΔV_p. The excited orbital state energies are indicated with arrows.

comes into resonance with μ in this step, the tunneling rate into the dot Γ_{in} drastically increases. This happens because the excited orbital states have a much stronger tunnel coupling to the reservoir than to the ground state. In the depicted range of energies, only one electron can occupy the dot at a time because the larger charging energy puts the dot into Coulomb blockade.

The tunneling rates into the excited orbital states are on the order of tens of kHz and thus not directly resolvable as they exceed the charge sensor bandwidth of 3 kHz. This issue is addressed by considering the pulse bandwidth of the gates, which is approximately 1 MHz: As depicted in Fig. 10a, in the charging step the excited orbital state is brought into resonance with μ for a time t_w, which is usually chosen on the order of tens to hundreds of μs. Here, an electron that occupies an excited orbital state will quickly decay into the ground state, which happens on a GHz timescale. After this fast decay, the electron is trapped in the ground state. Having waited for t_w in the protocol, the ground state is pulsed into resonance with μ for the readout step, where the charge sensor is monitored for 500 μs (corresponding to a timescale of 2 kHz). During the readout time, four different events can be distinguished on the charge sensor: The dot can either be loaded (if a tunneling event has occured during charging), emptied, have an electron tunnel into the empty dot or have it tunnel out of the dot. Because the intermediate tunneling rate of the ground state is tuned to below 100 Hz for this protocol, the last two events only make out a few percent of the signal and are neglected for the calculation of an occupation probability P_{on}. By scanning over different pulse detunings ΔV_p at a constant t_w, a plot such as shown in Fig. 10b is obtained, revealing the excited state energies $E_{x/y} = \alpha_p \cdot \Delta V_{p,E_{x/y}}$ in combination with the lever arm α_p. The exponential decay in P_{on} with increasing ΔV_p stems from the increasing tunnel barrier in the WKB approximation (see Sec. 3.4).

4 Results and discussion

This chapter presents the findings of this thesis. First, the determination of the lever arm that is essential for all subsequent results is shown in Sec. 4.1. Then, the excited orbital state measurements are presented in Sec.4.2, which allows to extract the shape parameters of the investigated quantum dot. Finally, the experimental challenges regarding the g-factor measurements are elucidated in Sec. 4.3, followed by the measured data for the corrections to the g-factor in Sec. 4.4.

4.1 Lever arm

Multiple measurements such as the one explained in Sec. 3.1 were carried out and from the fitted Fermi-Dirac distributions, values of the width ΔV_p for the central plunger gate CP were obtained at different temperatures T_{CF} of the cold finger thermometer. Choosing a point where T_e is assumed to be equivalent to T_{CF} [54], the lever arm α_p is then calculated using the relation

$$\alpha_p = \frac{k_B T_{CF}}{\Delta V_p}. \tag{22}$$

Using the values $k_B = 86.17\ \frac{\mu eV}{K}$, $T_{CF} = 658 \pm 5$ mK and $\Delta V_p = 1.07 \pm 0.06$ mV, a value of

$$\alpha_p = 53.06 \pm 2.80\ \frac{\mu eV}{mV}$$

is obtained (the detailed error propagation can be found in Appendix A.2). With this lever arm, the electron temperature $T_e = \frac{\alpha_p \Delta V_p}{k_B}$ can be extracted, which is shown in Fig. 11 in dependence of T_{CF}. At coldfinger temperatures above approximately 300 mK, $T_e \approx T_{CF}$. Approaching the base temperature at lower T_{CF}, T_e begins to deviate from T_{CF} due to parasitic heat leaks. For a point close to the refrigerator

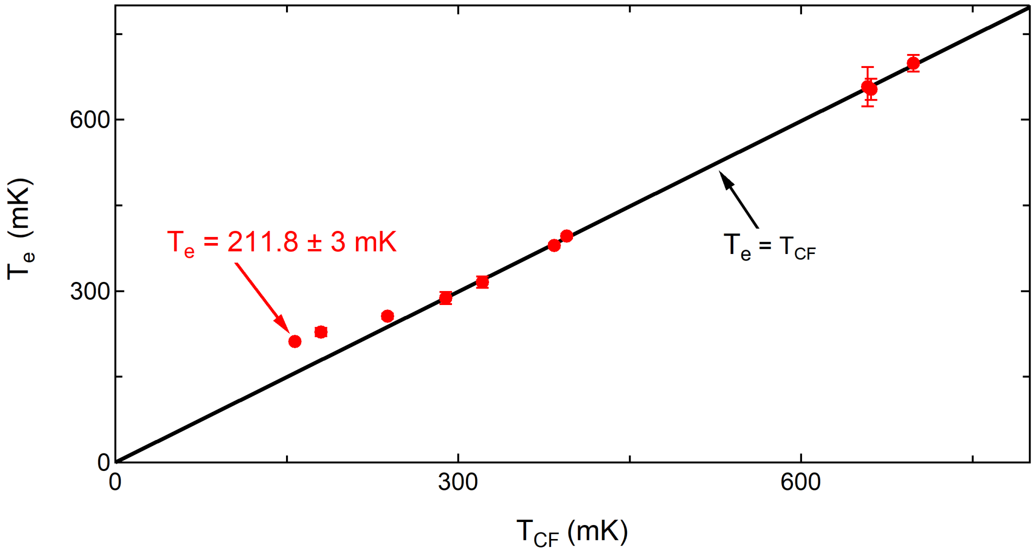

Figure 11: Electron temperature T_e (red dots) in dependence of the cold finger temperature T_{CF}. The solid black line corresponds to $T_e = T_{CF}$. At cold finger temperatures below approximately 300 mK, T_e is found to be higher than T_{CF}. The error bars are obtained from the error propagation in Appendix A.2.

base temperature, reading $T_{CF} = 156.6$ mK, a width $\Delta V_p = 0.34 \pm 0.01$ mV was measured. Applying the above calculated lever arm to this gives an electron temperature $T_e = 212 \pm 3$ mK.

4.2 Excited orbital states

In order to determine the shape properties of the investigated quantum dot, measurements of the excited orbital states were done as a function of the magnetic field. While the g-factor corrections only show a weak dependence on the two-dimensional shape of the quantum dot in the 2DEG plane (i.e. E_x and E_y) [12], a strong dependency on the width l_z can be observed in Fig. 6a and 6c. Therefore, extracting E_z from the excited orbital state data is also important for the analysis of the g-factor corrections.

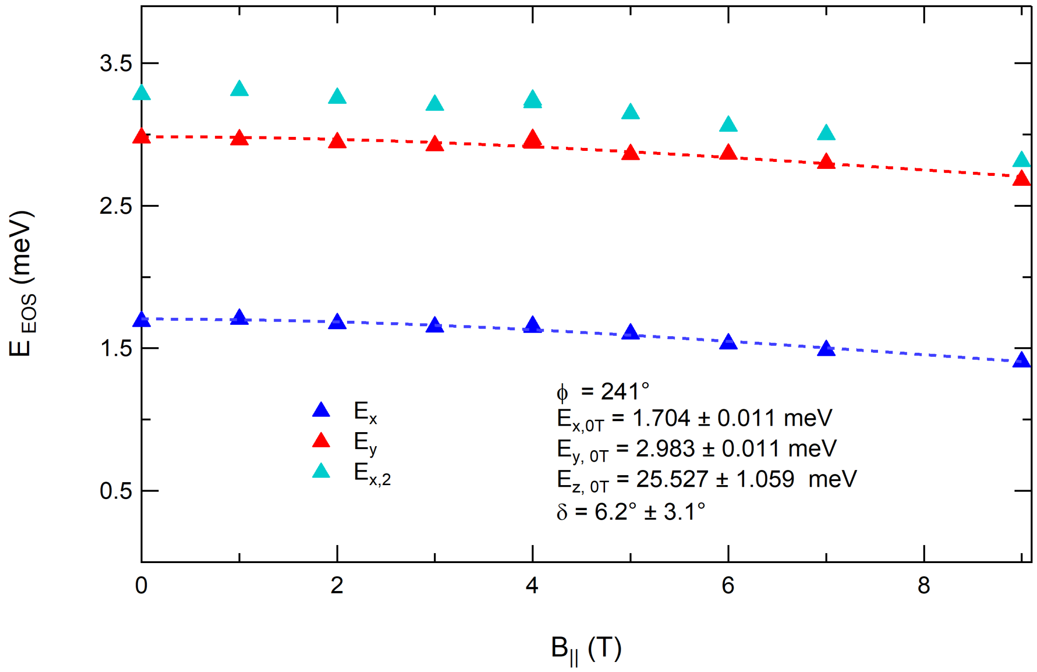

Figure 12: Excited orbital state energies E_{EOS} for different in-plane magnetic fields $B_{||}$ in the direction $\phi = 241°$, along with the extracted parameters from the fit to Eq. (23) (dashed curves). In this range of energies, the three orbital energies E_x, E_y and $E_{x,2}$ are visible. Here, $E_{x,2}$ is the second harmonic of E_x, δ the angle of the quantum dot axes relative to [1 0 0] and the energy E_z contains information on the 2DEG width.

Fig. 12 shows the measured excited orbital energies as a function of the in-plane magnetic field $B_{||}$ for an angle $\phi = 241°$ relative to the [1 0 0] direction. The spatial extent of the quantum dot wave function can be determined in all three dimensions by fitting the excited orbital energies E_{n_x} and E_{n_y} with the equation

$$\delta E_{n_x,n_y} = -\frac{\Phi^2}{2}\left[\hbar\omega_x sin^2(\delta-\phi)(n_x+1/2) + \hbar\omega_y sin^2(\delta+\pi/2-\phi)(n_y+1/2)\right]. \tag{23}$$

Here, it is assumed that the flux due to the in-plane field $\Phi = \frac{e}{\hbar}B\lambda_z^2$ (which is specifically defined for Ref. [12, 39]), with λ_z the effective width of the wave function along $\hat{z}$, is far smaller than 1, and that inter-subband corrections can be neglected as only the lowest subband of the 2DEG is occupied [28, 32]. The obtained energies $\hbar w_i$ correspond to the case B = 0 T. By using the relation $\hbar w_i = \hbar^2/(m^* l_i^2)$, the lengths l_i of the quantum dot can then be calculated, resulting in the values

$$l_x = 25.84 \pm 0.08 \text{ nm}, \quad l_y = 19.53 \pm 0.04 \text{ nm}, \quad l_z = 6.68 \pm 0.14 \text{ nm}.$$

Here, the uncertainties are the standard deviations obtained from the fit. The parameter $\delta = 6.2° \pm 3.1°$, which describes the in-plane angle of the quantum dot axes relative to the [1 0 0] direction, is close to zero with a high relative uncertainty. For a quantum dot whose x-orbital is aligned with the $\hat{x}$ direction, this angle is $\delta = 45°$. In order to determine this angle more reliably, more extensive measurements of E_x and E_y in dependence of the in-plane angle ϕ would be necessary, as it was done in Ref. [32]. In that work, a smaller 2DEG width $l_z = 6.3 \pm 0.3$ nm was determined.

When comparing the excited state energies $E_x \approx 1.7$ meV and $E_y \approx 3$ meV, it is recognized that one of the energies noticeably exceeds the other, such that the quantum dot here is very close to the condition $E_y \approx 2E_x$. In such a case, the quantum dot is strongly elongated in one direction, hence why this regime is referred to as a quasi-one-dimensional dot. A very interesting property of such a dot geometry is that the field-induced corrections to E_x and E_y are predicted to be in phase with respect to the in-plane angle ϕ (see Fig. 4c and 4d of Ref. [39]). In stark contrast to this, the corrections for a symmetric dot (where $E_x \approx E_y$) in dependence of ϕ are phase-shifted by 180°. However, for the g-factor corrections that are the central topic of this thesis, the theory predicts that the dot shape only has a weak effect [12].

4.3 Challenges during the g-factor measurements

There are several factors that made measuring the g-factors a challenging task. With increasing magnetic field, the tunneling rate was observed to decrease. To compensate this, the gates which define the tunnel barrier of the dot were tuned to slightly less negative voltages (within tens of mV) for increasing magnetic fields, which could sometimes make the quantum dot unstable. For example, in certain gate configurations the quantum dot was subjected to low frequency charge noise (switchers) that occurred on a time scale of a few hours, such that it was suddenly no longer possible to track the transition with the drift compensation mechanism explained in Sec. 3.2. Overall, the sample was only stable for a narrow parameter space in gate voltages and it was not possible to tune the elongated quantum dot to a more symmetric shape.

The sample that was investigated in this thesis was fabricated on a wafer with different properties (see Sec. 3) than the one used for the first device in Ref. [1], which had a dopant density of $n_\delta = 6 \cdot 10^{12}$ cm^{-2}, a mobility of $\mu = 4 \cdot 10^5 \frac{cm^2}{V s}$ and a 2DEG density of $n = 2.6 \cdot 10^{11}$ cm^{-2}. The 2DEG was less stable, such that the success rate of the measurements in this thesis was lower than in the previous experiment. Furthermore, a sizeable amount of measurements were not useful because they showed additional resonances of the tunneling rate in dependence of the plunger gate voltage such as the one shown in Fig. 13, thus preventing the identification of the excited spin state. These resonances could originate from localization effects in the electron reservoir (which could be further increased due to the slightly lower mobility of this sample compared to the previous experiment): In combination with the confinement of the depletion gates close to the tunnel barrier, the low-dimensional character of the localization effects could modulate the density of states in the reservoir. As a result, the density of states could deviate from the energy-independent 2D density of states (Eq. (2.1)) and gain an energy-dependence, which would manifest itself as additional resonances of the tunneling rate [52]. In order to avoid these reservoir artefacts, measurements in which they appeared were repeated at slightly altered gate configurations until the two spin states could be distinguished. This succeeded most of the time through a change of gate voltage at the left SEP gate of the reservoir (see Fig. 2a) within a range of

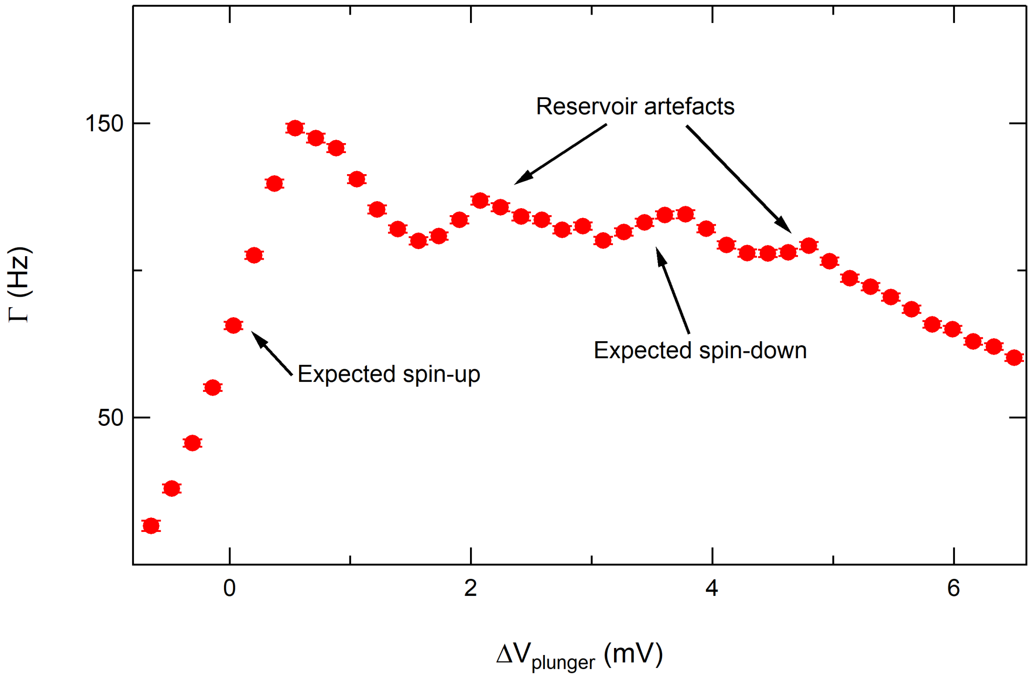

Figure 13: Example of a tunneling rate measurement ($\phi = 270°$, $B = 7.5$ T), showing the additional reservoir artefacts which interfere with the extraction of the Zeeman splitting. The expected voltages of the two spin states are indicated with arrows.

100 mV (tuning the gate beyond this range was avoided in order to leave the lever arm α_p unchanged). The reason as to why this works could be that too negative gate voltages at the reservoir could give it a point-like character, thereby increasing the presence of reservoir artefacts. In cases where changing the SEP gate voltage was also unsuccessful, measurements were repeated at a slightly different magnetic field strength.

In the data, the decrease in the spin tunneling asymmetry factor χ with an increasing magnetic field as proposed by Amasha et al. [50] could also be observed on a qualitative level. This behaviour made it harder to fit to the second spin state at high magnetic field as it became increasingly obscured by smaller resonances. Additionally, it was observed that changing the gate voltages of the tunnel barrier (gates LW and N) while staying at the same magnetic field strength could change the measured χ. Overall, the suppressed χ along with the reservoir artefacts led to higher fitting errors for the extracted Zeeman splittings. Furthermore, the acquisition of data points at high magnetic fields above 10 T was difficult due to increased noise levels due to pump vibrations coupling into the fridge.

4.4 g-factor corrections

From fits through tunneling rate measurements such as the one presented in Fig. 9d, the Zeeman splittings were obtained for different magnetic field directions and strengths. The uncertainties for the energy difference were obtained from the fitting errors (see Appendix A.2).

By plotting ΔE_Z against $\mu_B B$ and performing a linear fit to the data, the absolute value of the g-factor is obtained as the slope. An example is shown in Fig. 14 for the magnetic field direction along $[1\,\bar{1}\,0]$. Considering the angle ϕ from the theory which is defined with respect to the $[1\,0\,0]$ direction (see inset of Fig. 15), the direction $[1\,\bar{1}\,0]$ corresponds to $\phi = 315°$. Under the assumption that the corrections follow a sinusoidal behaviour with a periodicity of 180° (see Fig. 7a), the g-factor for this direction is considered as equivalent to the one at $\phi = 135°$. In the presented plot, an absolute value of $|g| = 0.365 \pm 0.006$ was obtained. The relative uncertainties in the Zeeman splitting and thus g-factor are on the order of a few percent, owing to the fairly large fitting errors $\delta(\Delta V_Z)$ for some data points (see Appendix A.3 for the individual data points), along with a low number of data points for each field direction. Here, problems with reservoir artefacts that masked the excited spin tunneling peak led to a decreased number of useful data points (see Sec. 4.3). The uncertainty bounds could be further reduced by taking even more data points, e.g. by measuring smaller steps in the magnetic field in order to bypass some of the reservoir artefacts.

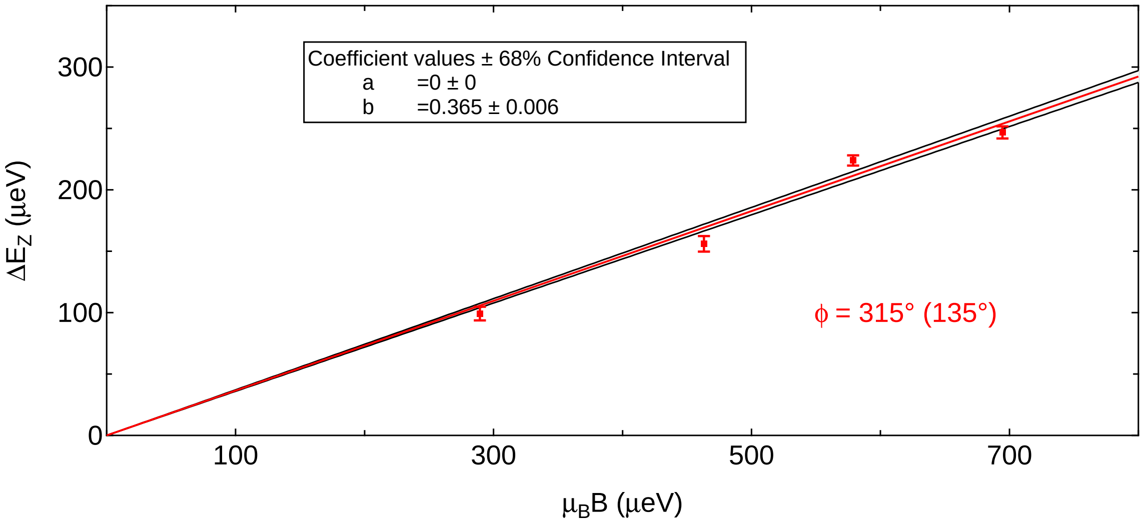

Figure 14: Extracted Zeeman splittings ΔE_Z, plotted against $\mu_B B$ for magnetic fields of 5, 8, 10 and 12 Tesla. The error bars are obtained from the statistical uncertainty of the fits (see Appendix A.2). The angle $\phi = 315°$ corresponds to a magnetic field in the $[1\,\bar{1}\,0]$ $(\hat{y})$ direction. Doing a linear fit through the data (red line) reveals the absolute value of the dimensionless g-factor as the slope, along with a statistical uncertainty. The confidence band within one standard deviation is indicated with black lines.

The extraction of the g-factor for different angles ϕ shows an anisotropy of the g-factor, with values ranging from $|g| \approx 0.365$ for $\phi = 315°$ to $|g| \approx 0.415$ for $\phi = 241°$ (the corresponding fits are shown in Appendix A.4). The different g-factors, along with an additional data point for $\phi = 225°$ that was measured in the same device during the writing process of this thesis, are plotted in Fig. 15. In order to allow comparison to the predicted corrections from Ref. [12] (see Sec. 2.4), the g-factor corrections are separated into an anisotropic correction δg_a and an isotropic correction δg_i that are applied to the bulk g-factor $g_{bulk} = -0.44$, i.e.

$$g = g_{bulk} + \delta g_i + \delta g_a \cdot sin(2\phi + \pi). \tag{24}$$

By fitting a sinusoidal function through the extracted g-factors for different ϕ (see Appendix A.5), a mean value of $|\bar{g}| = 0.396 \pm 0.003$ is obtained. From theory, this mean value is considered to only include the isotropic correction to the bulk g-factor, such that $\delta g_i = 0.044 \pm 0.003$. This result is considerably lower than the theoretical prediction $\delta g_{i,theory} \approx 0.11$ (see Fig. 6d). Furthermore, the amplitude of the sinusoidal fit is taken as the anisotropic correction, yielding $\delta g_a = 0.025 \pm 0.004$, which is reasonably close to the predicted $\delta g_{a,theory} \approx 0.024$ (see Fig. 7a). The anisotropic correction δg from $\bar{g} \approx -0.396$ is shown in dependence of ϕ in Fig. 16. Although the uncertainties for the extracted g-factor are significant

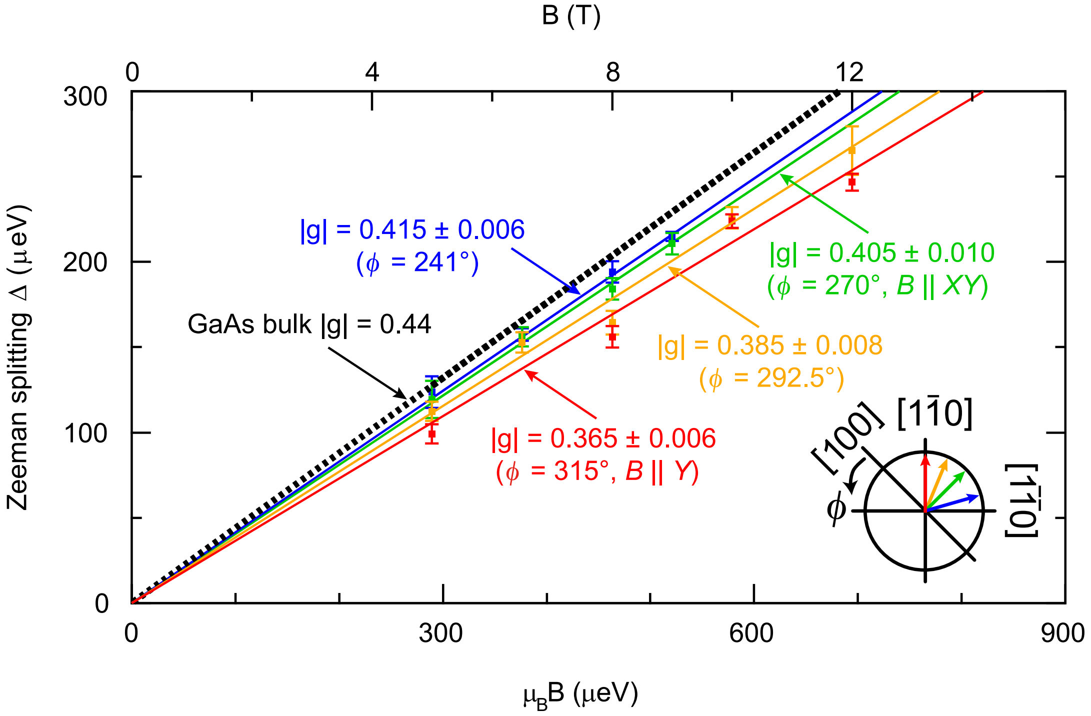

Figure 15: Extracted Zeeman splittings ΔE_Z for different strengths and directions of the in-plane magnetic field B, showing a noticeable anisotropy of the g-factor. The fits for the extracted g-factors (solid lines) and the GaAs bulk g-factor (dashed line) are also shown. Corresponding crystallographic directions of the measurements are indicated with colors in the inset.

compared to the magnitude of the prediction, a clear trend can be observed between the data for the $[1\,\bar{1}\,0]$ direction and the data close to the $[\bar{1}\,\bar{1}\,0]$ direction. Considering the relative correction to the g-factor, a ratio $\delta g_a/|\bar{g}| = 6.3 \pm 0.8\%$ is obtained, which is very close to the theoretical prediction of 7%.

Here, it needs to be noted that the theoretical predictions were made for a wafer with different properties that was used to fabricate the first device in Ref. [1] (see Sec. 4.3). The quantum dot on that wafer was also more stable than the one that was investigated in this thesis. Measurements on this other sample yielded values of $|\bar{g}| = 0.373 \pm 0.001$, $\delta g_i = 0.067 \pm 0.001$, $\delta g_a = 0.030 \pm 0.002$ and a ratio $\delta g_a/|\bar{g}| = 8.1 \pm 0.5\%$. The anisotropic behaviour of the g-factor in that sample is also plotted in Fig. 16. The uncertainties in g-factor for that sample were smaller than for the sample measured in this thesis. A reason for this is that the measurements presented in this thesis have a lower amount of data points for each field direction. Conversely, there were more different field directions measured in the device of this thesis than in the previous device.

While the measured values for the anisotropic correction δg_a are reasonably close to the prediction, the measured isotropic correction δg_i is only about 40% of the predicted value. Considering the plot for the predicted corrections in dependence of l_z (Fig. 6c), one expects such an isotropic correction at $l_z \approx 13$ nm instead of the width $l_z \approx 6.7$ nm that was obtained in the measurement of the excited orbital states (Sec. 4.2). Also, repeating this procedure for the other device with $\delta g_i \approx 0.07$ leads to $l_z \approx 10$ nm instead of the width $l_z \approx 6.3$ nm that was obtained in Ref. [32] in a more thorough measurement. For both devices, the widths l_z that would be obtained from the isotropic correction alone are in a regime

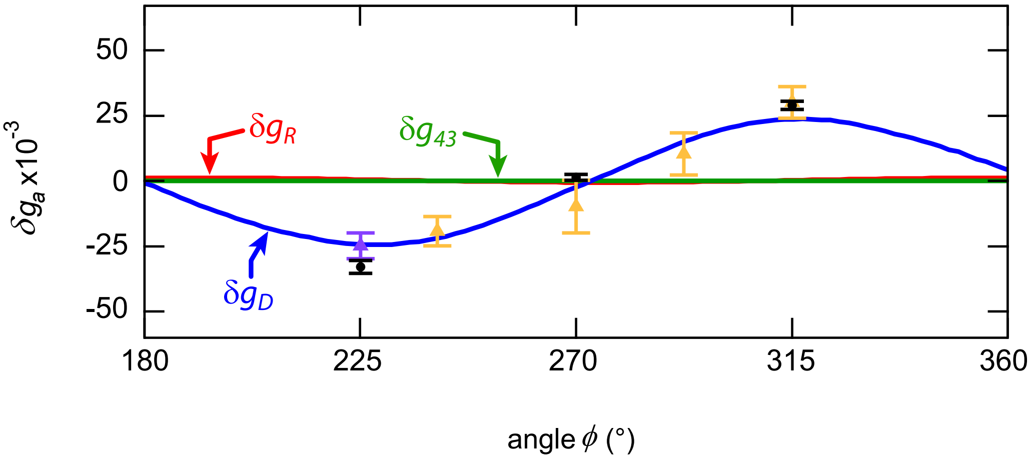

Figure 16: Theoretical predictions for the anisotropic g-factor correction g_D along with the isotropic corrections g_{43} and g_R. The g-factor data measured in this thesis (yellow triangles), along with a data point for $\phi = 225°$ (purple triangle) which was measured in the same device during the writing process of this thesis. Together with the experimental data from the preceding device [1] (black dots), the data points are plotted on top of the prediction, showing good agreement with the theory. The error bars are obtained from the fitting errors.

where the g-factor corrections δg_d and δg_r are predicted to become strongly suppressed at increasing magnetic field as can be seen in Figs. 6c and 6d. Such a behaviour was not observed in the experiments, where the Zeeman splitting was measured to be linear over a large range of magnetic fields.

There are several possible sources that could contribute to the above described discrepancies. First, the large uncertainty of $\approx \pm 5\%$ in the lever arm increases the uncertainty of the extracted g-factors. For example, a smaller lever arm would decrease $|\bar{g}|$ and δg_a while increasing δg_i. Furthermore, it could be that despite selecting for data without reservoir artefacts, some of the extracted Zeeman splittings could still be altered by this effect. Looking at the data in Fig. 14 and Appendix A.4, there are indeed some points that do not fit nicely on the g-factor slope and even come too close to the slopes at other directions, as can be seen in Fig. 15.

Besides the experimental limitations, there are also possible sources of deviations in the theoretical model. Here, the negligence of strain-induced SOI and simplifications in the heterostructure confinement potential could lead to further corrections to the theory [28]. Furthermore, there might be inconsistencies in the $\mathbf{k} \cdot \mathbf{p}$ constants used for the model [12]: Considering again the plot in Fig. 6c and fixing the width at $l_z \approx 6.7$ nm from the excited orbital state data, it is seen that the measured total isotropic correction $\delta g_i \approx 0.044$ is weaker than both predicted isotropic corrections $\delta g_r \approx 0.07$ and $\delta g_{43} \approx 0.05$. Under the assumption that δg_r and δg_d are better established in theory than δg_{43}, the data suggests that δg_{43} has a negative sign. Applying the same thought process to the other device, a value $\delta g_{43} \approx 0$ would be obtained there.

5 Conclusions and outlook

A wide array of pulse-gate spectroscopy techniques was used in order to characterize the shape and g-factors of a quantum dot in a single-electron spin qubit device. The characterization of the excited orbital states allowed to determine a 2DEG width $l_z = 6.68 \pm 0.14$ nm. Furthermore, it turned out that the investigated quantum dot is elongated along one direction, which is an interesting regime due to the changing behaviour of the orbital energies with respect to the direction of the in-plane magnetic field. The investigated sample was less ideal than its predecessor due to the reduced mobility and a higher incidence of switchers. Despite these experimental challenges, a statistically significant g-factor anisotropy could be measured, showing values between $|g| = 0.365 \pm 0.006$ and $|g| = 0.415 \pm 0.006$ when the in-plane angle ϕ is varied within a range of 74°. The observed behaviour is in agreement with the theory by Stano et al. [12], which predicts an anisotropic correction originating from the Dresselhaus SOI (g_d) along with an isotropic correction arising mainly from the Rashba SOI term (g_r) and the bulk SOI term H_{43} (g_{43}). While the measured anisotropic correction δg_a was found to be in well agreement with the prediction, the isotropic correction δg_i was determined to be only approximately 40% of its predicted value.

Together with the previous data for a different wafer, the presented results could help determining the $\mathbf{k} \cdot \mathbf{p}$ parameters that are relevant for the calculation of such g-factor corrections with an increased accuracy. Because these parameters are known to depend strongly on the 2DEG width l_z, this research could be extended by investigating samples with a higher l_z. For example, in the regime $l_z > 10$ nm it is predicted that the corrections to the g-factor decrease by an order of magnitude.

The presented experiment is limited by a few factors. First, the observed reservoir artefacts in the tunneling rate data combined with the sometimes strongly suppressed spin tunneling asymmetry factor χ led to a small success ratio of below 20% for the measurements. Because a measurement could take up to 10 hours in total for one configuration, the measurement efficiency was quite low. To address this, it should be possible to decrease the point-like character of the tunnel-coupled reservoir as was done in Ref. [52], thereby reducing the amount of reservoir artefacts in the measured data. Second, the experiment is limited by the systematic uncertainty of the lever arm of approximately 5% (see Appendix A.2), which acts globally on the set of obtained g-factors. Despite this limitation on the accuracy of the measurements, it is nonetheless possible to achieve a high precision, making it possible to resolve the small changes in the g-factor with the field direction and thereby characterize the g-factor anisotropy. Thinking beyond this experiment, the obtained resolution of g-factor measurements could be improved by doing an electric dipole spin resonance (EDSR) experiment such as described in Ref. [55], which allows to extract the g-factor with an even higher resolution. Though, the shaking of the electron in one direction that would occur in such an experiment might also affect the measurement of the g-factor anisotropy and would possibly also need to be addressed by the theory. Furthermore, the application of pulses in the range of GHz in such an experiment could also affect properties of the quantum dot such as the charge stability. Nonetheless, doing either an EDSR experiment or a measurement of the spin relaxation time T_1 as was done in Ref. [14] would also allow to extract the corrections g_d and g_r, which can be indirectly used to quantify the magnitude of g_{43}.

Finally, it should be emphasized that, together with the measurements in the preceding device with this setup [1], the measurements presented in this thesis constitute the first experiment where the g-factor anisotropy has ever been determined within the same GaAs spin qubit devices. As such, this knowledge on the behaviour of the g-factor is a valuable ingredient for the operation of spin qubits.

6 Acknowledgements

First and foremost, I would like to thank Prof. Dominik Zumbühl for granting me the possibility to do this Master's thesis in his group. The time spent here allowed me to acquire a wide variety of knowledge, such as the technical skills that I learned by working in the cryolab or the fruitful discussions and talks in the group meeting that gave me a broader insight into current research topics in the field of quantum transport. Special thanks go to Leon Camenzind, who supervised this project and aided me during the whole process, starting with the initial fixing process of the fridge, providing of the sample, the implementation of the measurement methods and thorough explanations that helped me understand the theory better.

I am also grateful to Peter Stano from RIKEN, who provided the theoretical backbone to this work and also calculated the g-factor corrections for the specific case of an elongated quantum dot. Special thanks also go to Liuqi Yu, who fabricated the devices. Furthermore, I would like to thank the former and current members of the Zumbühl group that were present during my master's thesis - Christian Scheller, Floris Braakman, Mohammad Samani, Taras Patlatiuk, Florian Froning, Timothy Camenzind, Kris Cerveny, Miguel Carballido, Henok Weldeyesus, Omid Sharifi, Fabian Müller, Mirko Rehmann, Bilal Kalyoncu, Qianqian Chen and Luk Yi Cheung, which all contributed to a very pleasant working atmosphere in the group.

Further thanks go to the Michael Steinacher and Sascha Lindner from the electronics workshop of the department, which helped us solve problems with the electronics in the setup. Also, I would like to thank Dominik Sifrig and Patrick Stöcklin from the mechanical workshop, without whose work at the helium liquefier it wouldn't be possible to do the experiments. Additionally, I would like to say thank you to Barbara Kammermann, Astrid Kalt and Stephan Weitnauer for their administrative work at the department.

Last but not least, I would like to thank my family for supporting me during all this time.

7 References

[1] L. C. Camenzind, S. Svab, P. Stano, L. Yu, J. D. Zimmerman, A. C. Gossard, D. Loss, and D. M. Zumbühl. Isotropic and Anisotropic g-factor Corrections in GaAs Quantum Dots. *arXiv:2010.11185*, (2020).

[2] G. E. Moore. Cramming more components onto integrated circuits. *Electronics* ***38***, *8*, (1965).

[3] R. P. Feynman. Simulating physics with computers. *Int. J. Theor. Phys.* ***21***, *467*, (1982).

[4] D. P. DiVincenzo. The physical implementation of quantum computation. *Fortschritte der Physik* ***48***, *771*, (2000).

[5] D. Loss and D. P. DiVincenzo. Quantum computation with quantum dots. *Phys. Rev. A* ***57***, *120*, (1998).

[6] M. Ciorga, A. S. Sachrajda, P. Hawrylak, P. Zawadzki C. Gould, S. Jullian, Y. Feng, and Z. Wasilewski. Addition spectrum of a lateral dot from coulomb and spin-blockade spectroscopy. *Phys. Rev. B* ***61***, *R16315*, (2000).

[7] W. Lu, Z. Ji, L. Pfeiffer, K. W.West, and A. J. Rimberg. Real-time detection of electron tunnelling in a quantum dot. *Nature* ***423***, *422*, (2003).

[8] J. M. Elzerman, R. Hanson, L. H. W. van Beveren, B. Witkamp, L. M. K. Vandersypen, and L. P. Kouwenhoven. Single-shot read-out of an individual electron spin in a quantum dot. *Nature* ***430***, *431*, (2004).

[9] R. Hanson, L. H. W. van Beveren, I. T. Vink, J. M. Elzerman, W. J. M. Naber, F. H. L. Koppens, L. P. Kouwenhoven, and L. M. K. Vandersypen. Single-shot readout of electron spin states in a quantum dot using spin-dependent tunnel rates. *Phys. Rev. Lett.* ***94***, *196802*, (2005).

[10] F. H. L. Koppens, C. Buizert, K. J. Tielrooij, I. T. Vink, K. C. Nowack, T. Meunier, L. P. Kouwenhoven, and L. M. K. Vandersypen. Driven coherent oscillations of a single electron spin in a quantum dot. *Nature* ***442***, *766*, (2006).

[11] J. R. Petta, A. C. Johnson, J. M. Taylor, E. A. Laird, A. Yacoby, M. D. Lukin, C. M. Marcus, M. P. Hanson, and A. C. Gossard. Coherent manipulation of coupled electron spins in semiconductor quantum dots. *Science* ***309***, *5744*, (2005).

[12] P. Stano, C. H. Hsu, M. Serina, L. C. Camenzind, D. M. Zumbühl, and D. Loss. g-factor of electrons in gate-defined quantum dots in a strong in-plane magnetic field. *Phys. Rev. B* ***98***, *195314*, (2018).

[13] T. Tanttu, B. Hensen, K. W. Chan, C. H. Yang, W. W. Huang, M. Fogarty, F. Hudson, K. Itoh, D. Culcer, A. Laucht, A. Morello, and A. Dzurak. Controlling spin-orbit interactions in silicon quantum dots using magnetic field direction. *Phys. Rev. X* ***9***, *021028*, (2019).

[14] L. C. Camenzind, L. Yu, P. Stano, J. D. Zimmerman, A. C. Gossard, D. Loss, and D. M. Zumbühl. Hyperfine-phonon spin relaxation in a single-electron gaas quantum dot. *Nat. Commun.* ***9***, *3454*, (2018).

[15] A. V. Khaetskii and Y. V. Nazarov. Spin-flip transitions between zeeman sublevels in semiconductor quantum dots. *Phys. Rev. B.* ***64***, *125316*, (2001).

[16] R. Hanson, L. P. Kouwenhoven, J. R. Petta, S. Tarucha, and L. M. K. Vandersypen. Spins in few-electron quantum dots. *Rev. Mod. Phys.* ***79**, 1217*, (2007).

[17] F. K. Malinowski, F. Martins, P. D. Nissen, E. Barnes, Ł. Cywinski, M. S. Rudner, S. Fallahi, G. C. Gardner, M. J. Manfra, C. M. Marcus, and F. Kuemmeth. Notch filtering the nuclear environment of a spin qubit. *Nat. Nanotechnol.* ***12**, 16*, (2017).

[18] S. G. Carter, T. M. Sweeney, M. Kim, C. S. Kim, D. Solenov, S. E. Economou, T. L. Reinecke, L. Yang, A. S. Bracker, and D. Gammon. Quantum control of a spin qubit coupled to a photonic crystal cavity. *Nat. Phot.* ***7**, 329*, (2013).

[19] M. Veldhorst, J. C. C. Hwang, C. H. Yang, A. W. Leenstra, B. de Ronde, J. P. Dehollain, J. T. Muhonen, F. E. Hudson, K. M. Itoh, A. Morello, and A. S. Dzurak. An addressable quantum dot qubit with fault-tolerant control-fidelity. *Nat. Nanotechnol.* ***9**, 981*, (2014).

[20] Y. Yang, S. N. Coppersmith, and M. Friesen. Achieving high-fidelity single-qubit gates in a strongly driven charge qubit with 1/f charge noise. *npj Quantum Inf.* ***5**, 12*, (2019).

[21] R. M. Potok, J. A. Folk, C. M. Marcus, V. Umansky, M. Hanson, and A. C. Gossard. Spin and polarized current from coulomb blockaded quantum dots. *Phys. Rev. Lett.* ***91**, 016802*, (2003).

[22] R. Hanson, B. Witkamp, L. M. K. Vandersypen, L. H. Willems van Beveren, J.M. Elzerman, and L. P. Kouwenhoven. Zeeman energy and spin relaxation in a one-electron quantum dot. *Phys. Rev. Lett.* ***91**, 196802*, (2003).

[23] D. Goldhaber-Gordon, H. Shtrikman, D. Mahalu, D. Abusch-Magder, U. Meirav, and M. A. Kastner. Kondo effect in a single-electron transistor. *Nature* ***391**, 156*, (1998).

[24] A. Kogan, S. Amasha, D. Goldhaber-Gordon, G. Granger, A. Kastner, and H. Shtrikman. Measurements of Kondo and spin splitting in single-electron transistors. *Phys. Rev. Lett.* ***93**, 166602*, (2004).

[25] L. P. Kouwenhoven S. M. Cronenwett, T. H. Oosterkamp. A tunable Kondo effect in quantum dots. *Science* ***281**, 540*, (1998).

[26] D. M. Zumbühl and C. M. Marcus. Cotunneling spectroscopy in few-electron quantum dots. *Phys. Rev. Lett.* ***93**, 256801*, (2004).

[27] V. P. Michal, T. Fujita, T. A. Baart, J. Danon, C. Reichl, W. Wegscheider, L.M.K. Vandersypen, and Y. V. Nazarov. Non-linear and dot-dependent zeeman splitting in gaas/algaas quantum dot arrays. *Phys. Rev. B* ***97**, 035301*, (2018).

[28] L. C. Camenzind. *Spins and Orbits in Semiconductor Quantum Dots.* PhD thesis, University of Basel, 2019.

[29] T. Ihn. *Semiconductor Nanostructures: Quantum States and Electronic Transport.* Oxford University Press, 2010.

[30] R. J. Warburton. Self-assembled semiconductor quantum dots. *Cont. Phys.* ***43**, 351*, (2002).

[31] L. P. Kouwenhoven, D. G. Austing, and S. Tarucha. Few-electron quantum dots. *Rep. Prog. Phys.* ***64**, 701*, (2001).

[32] L. C. Camenzind, L. Yu, P. Stano, J. D. Zimmerman, A. C. Gossard, D. Loss, and D. M. Zumbühl. Spectroscopy of quantum dot orbitals with in-plane magnetic fields. *Phys. Rev. Lett.* ***122**, 207701*, (2019).

[33] L. P. Kouwenhoven, T. H. Oosterkamp, M. W. S. Danoesastro, M. Eto, D. G. Austing, T. Honda, and S. Tarucha. Excitation spectra of circular, few-electron quantum dots. *Science* ***278**, 1788*, (1997).

[34] G. Dresselhaus. Spin-orbit coupling effects in zinc blende structures. *Phys. Rev.* ***100**, 2*, (1955).

[35] R. Winkler. *Spin-orbit Coupling Effects in Two-Dimensional Electron and Hole Systems*. Springer Tracts in Modern Physics, 2003.

[36] E. I. Rashba. Spin-orbit coupling effects in zinc blende structures. *J. El. Spec. Rel. Phen.* ***201**, 4*, (1960).

[37] Y. A. Bychkov and E. I. Rashba. Oscillatory effects and the magnetic susceptibility of carriers in inversion layers. *J. Phys. C* ***17**, 6039*, (1984).

[38] J. Fabian, A. Matos-Abiague, C. Ertler, P. Stano, and I. Zutic. Semiconductor spintronics. *Acta Phys. Slovaca* ***57**, 565*, (2007).

[39] P. Stano, C. Hsu, L. C. Camenzind, L. Yu, D. M. Zumbühl, and D. Loss. Orbital effects of a strong in-plane magnetic field on a gate-defined quantum dot. *Phys. Rev. B* ***99**, 085308*, (2019).

[40] L.M. Roth, B. Lax, and S. Zwerdling. Theory of optical magneto-absorption effects in semiconductors. *Phys. Rev.* ***114**, 90*, (1959).

[41] N. R. Ogg. Conduction-band g factor anisotropy in indium antimonide. *Proc. Phys. Soc.* ***89**, 431*, (1966).

[42] B. D. McCombe. Infrared studies of combined resonance in n-type InSb. *Phys. Rev.* ***181**, 1206*, (1968).

[43] M. Braun and U. Rössler. Magneto-optic transitions and nonparabolicity parameters in the conduction band of semiconductors. *J. Phys. C: Solid State Phys.* ***18**, 3365*, (1985).

[44] H. W. Jiang and Eli Yablonovitch. Gate-controlled electron spin resonance in GaAs/AlGaAs heterostructures. *Phys. Rev. Lett.* ***122**, 207701*, (2001).

[45] G. Salis, Y. Kato, K. Ensslin, D. C. Driscoll, A. C. Gossard, and D. D. Awschalom. Electrical control of spin coherence in semiconductor nanostructures. *Nature* ***414**, 619*, (2001).

[46] C. P. Scheller, S. Heizmann, K. Bedner, D. Giss, M. Meschke, D. M. Zumbühl, J. D. Zimmerman, and A. C. Gossard. Silver-epoxy microwave filters and thermalizers for millikelvin experiments. *Appl. Phys. Lett.* ***104**, 211106*, (2014).

[47] D. E. F. Biesinger. *Thermally Activated Charge Fluctuations in GaAs Double Quantum Dots*. PhD thesis, University of Basel, 2014.

[48] L. Casparis, M. Meschke, D. Maradan, A. C. Clark, C. P. Scheller, K. K. Schwarzwälder, J. P. Pekola, and D. M. Zumbühl. Metallic coulomb blockade thermometry down to 10 mk and below. *Rev. Sci. Instrum.* ***83**, 083903*, (2012).

[49] K. MacLean, S. Amasha, I. P. Radu, D. M. Zumbühl, M. A. Kastner, M. P. Hanson, and A. C. Gossard. Energy-dependent tunneling in a quantum dot. *Phys. Rev. Lett.* ***98**, 036802*, (2007).

[50] S. Amasha, K. MacLean, I. P. Radu, D. M. Zumbühl, M. A. Kastner, M. P. Hanson, and A. C. Gossard. Spin-dependent tunneling of single electrons into an empty quantum dot. *Phys. Rev. B* ***78**, 041306*, (2008).

[51] P. Stano and P. Jacquod. Spin-dependent tunneling into an empty lateral quantum dot. *Phys. Rev. B* ***82**, 125309*, (2010).

[52] M. Yamagishi, N. Watase, M. Hashisaka, K. Muraki, and T. Fujisawa. Spin-dependent tunneling rates for electrostatically defined GaAs quantum dots. *Phys. Rev. B* ***90**, 035306*, (2014).

[53] S. Amasha, K. MacLean, I. P. Radu, D. M. Zumbühl, M. A. Kastner, M. P. Hanson, and A. C. Gossard. Electrical control of spin relaxation in a quantum dot. *Phys. Rev. Lett.* ***100**, 046803*, (2008).

[54] D. Maradan, L. Casparis, T.-M. Liu, D. E. F. Biesinger, C. P. Scheller, D. M. Zumbühl, J. D. Zimmerman, and A. C. Gossard. Gaas quantum dot thermometry using direct transport and charge sensing. *J. Low Temp. Phys.* ***175**, 784*, (2014).

[55] K. C. Nowack, F. H. L. Koppens, Y. V. Nazarov, and L. M. K. Vandersypen. Coherent control of a single electron spin with electric fields. *Science* ***318**, 1430*, (2007).

A Appendix

A.1 Van der Pauw measurement

The in-plane magnetic field that is applied for the g-factor measurement can be significantly large, ranging up to 12 T. Because large out-of-plane components can lead to the formation of Landau levels, it is crucial to have a good alignment of the sample with the external field. To determine the out-of-plane angle ξ of the sample, a Van der Pauw measurement of the Hall resistance was made. Under knowledge of the Hall coefficient $R_{H,\perp}$ for an out-of-plane magnetic field, the dependence $R_{H,\|} = R_{H,\perp} \cdot sin(\xi)$ allows to extract ξ. Such measurements of $R_{H,\|}$ were repeated for different angles θ of the ANC piezo rotator, leading to the plot in Fig. A1 that shows the dependence of ξ on θ (to get the in-plane angle ϕ that is relevant for the theory, the relation $\theta = 495° - \phi$ is applied). Here, ξ has a periodicity of 360° in θ and is under 1.5° at its maximum around roughly $\theta = 300°$, which is close to the crystal direction $[\bar{1}\,0\,0]$.

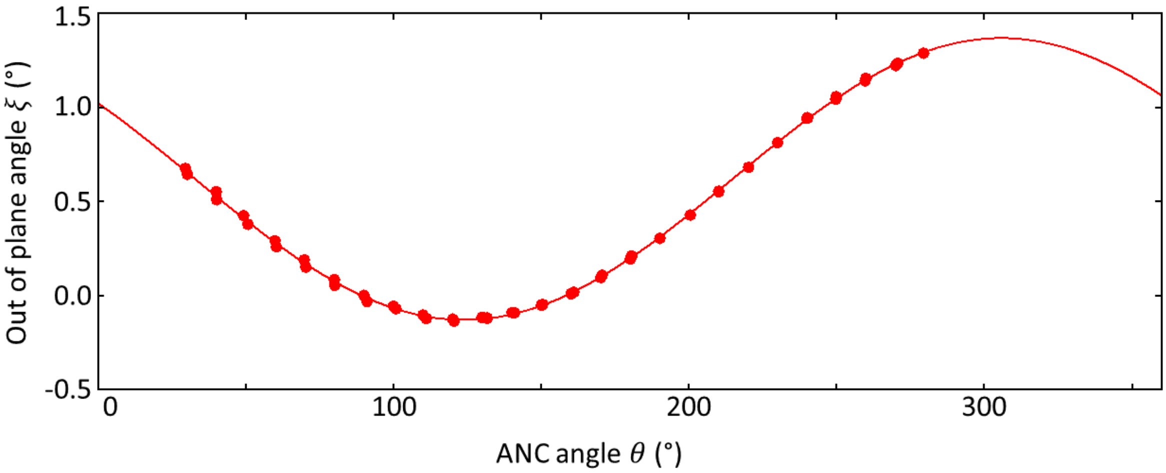

Figure A1: Extracted out-of-plane angle ξ from the Van der Pauw measurement in dependence of the angle θ of the piezo rotator. The measured points allow for a good sinusoidal fit with a 2π-periodicity.

A.2 Error propagation

A.2.1 Lever arm α_p

In order to estimate the uncertainty of the lever arm $\delta\alpha_p$ more accurately, a Gaussian error propagation can be performed with Eq. (22) while assuming that T_{CF} and ΔV_p are statistically independent from each other. This leads to the result

$$\delta\alpha_p = \sqrt{(\frac{\partial\alpha_p}{\partial(\Delta V_p)} \cdot \delta(\Delta V_p))^2 + (\frac{\partial\alpha_p}{\partial T_{CF}} \cdot \delta T_{CF})^2} = \sqrt{(\frac{-k_B T_{CF}}{(\Delta V_p)^2} \cdot \delta(\Delta V_p))^2 + (\frac{k_B}{(\Delta V_p)} \cdot \delta T_{CF})^2} \ ,$$

where $\delta(\Delta V_p)$ is the standard deviation obtained from the P_{on} measurement and $\delta T_{CF} = 5$ mK is an estimated systematic error from the AVS-47 temperature readout. Inserting $T_{CF} = 658$ mK, $\Delta V_p = 1.069$ mV and $\delta(\Delta V_p) = 0.056$ mV, one then obtains $\delta\alpha_p = 2.799 \ \frac{\mu eV}{mV}$, which is an uncertainty of approximately 5%. Here, it is worth noting that the uncertainty of the lever arm is a systematic effect, acting on the whole set of measured g-factors rather than on each individual value.

A.2.2 Zeeman splitting ΔE_Z

The uncertainty of the energy differences ΔE_Z is obtained by applying the lever arm α_p to the statistical uncertainty ΔV_Z of the fits through the tunneling rate measurement data: $\Delta E_Z = \alpha_p \Delta V_Z$. The uncertainty of the lever arm doesn't go into this calculation because it is a systematic effect that acts on the whole set of measured g-factors, thus limiting only the accuracy (closeness of a measurement to its true value), and not the precision (closeness of measurements to each other) of the measurements.

A.3 Measured Zeeman splittings

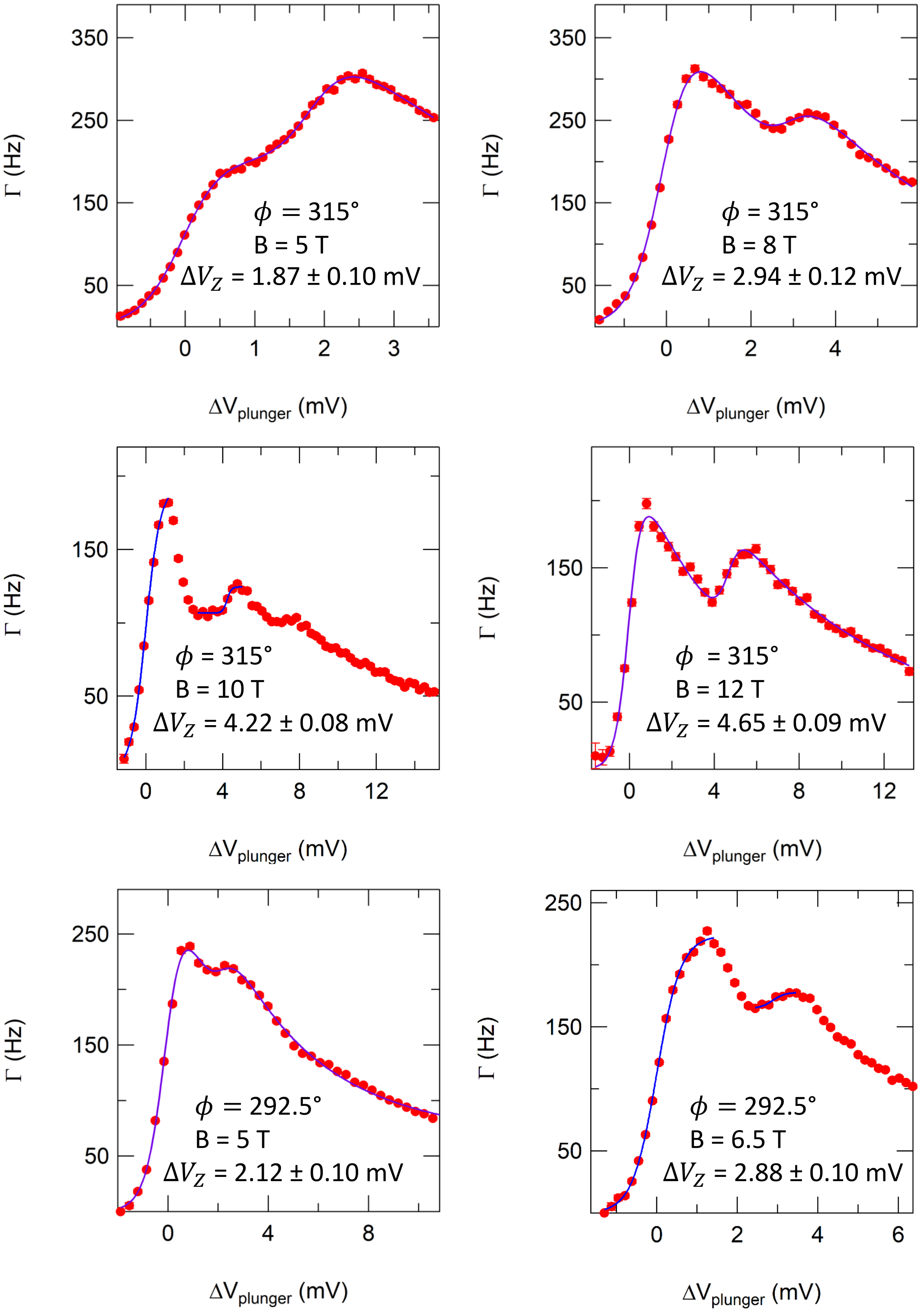

Figure A2: Data set #1 of the tunneling rate Γ in dependence of the pulsed plunger gate voltage $\Delta V_{plunger}$ for in-plane magnetic fields B at different angles ϕ. The voltage difference from the Zeeman splitting ΔV_Z was obtained from fits of either Eq. (19) with two different factors β (purple) for the two spin states or a sigmoid function (blue, disconnected fits).

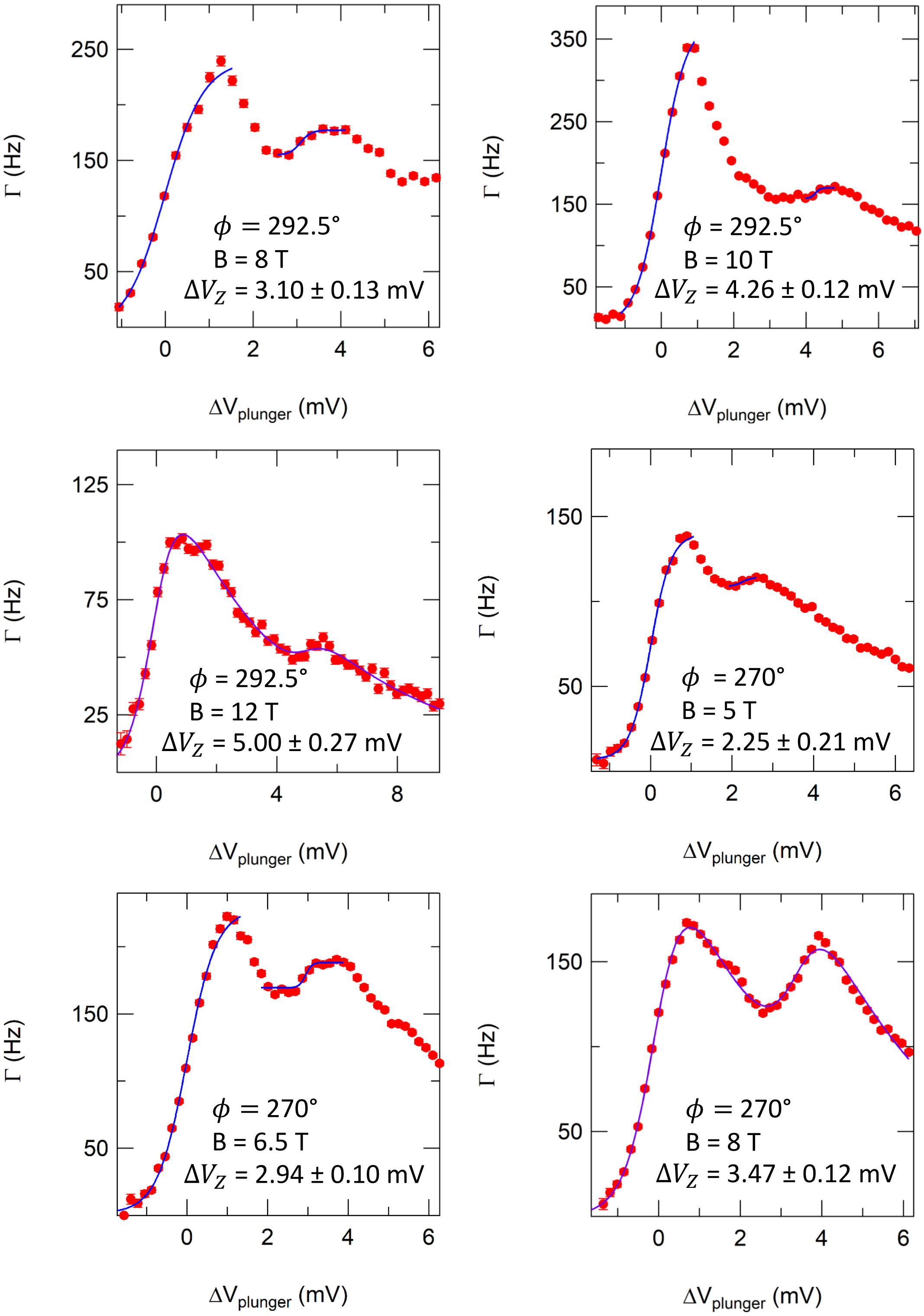

Figure A3: Data set #2 of the tunneling rate Γ in dependence of the pulsed plunger gate voltage $\Delta V_{plunger}$ for in-plane magnetic fields B at different angles ϕ. The voltage difference from the Zeeman splitting ΔV_Z was obtained from fits of either Eq. (19) with two different factors β (purple) for the two spin states or a sigmoid function (blue, disconnected fits).

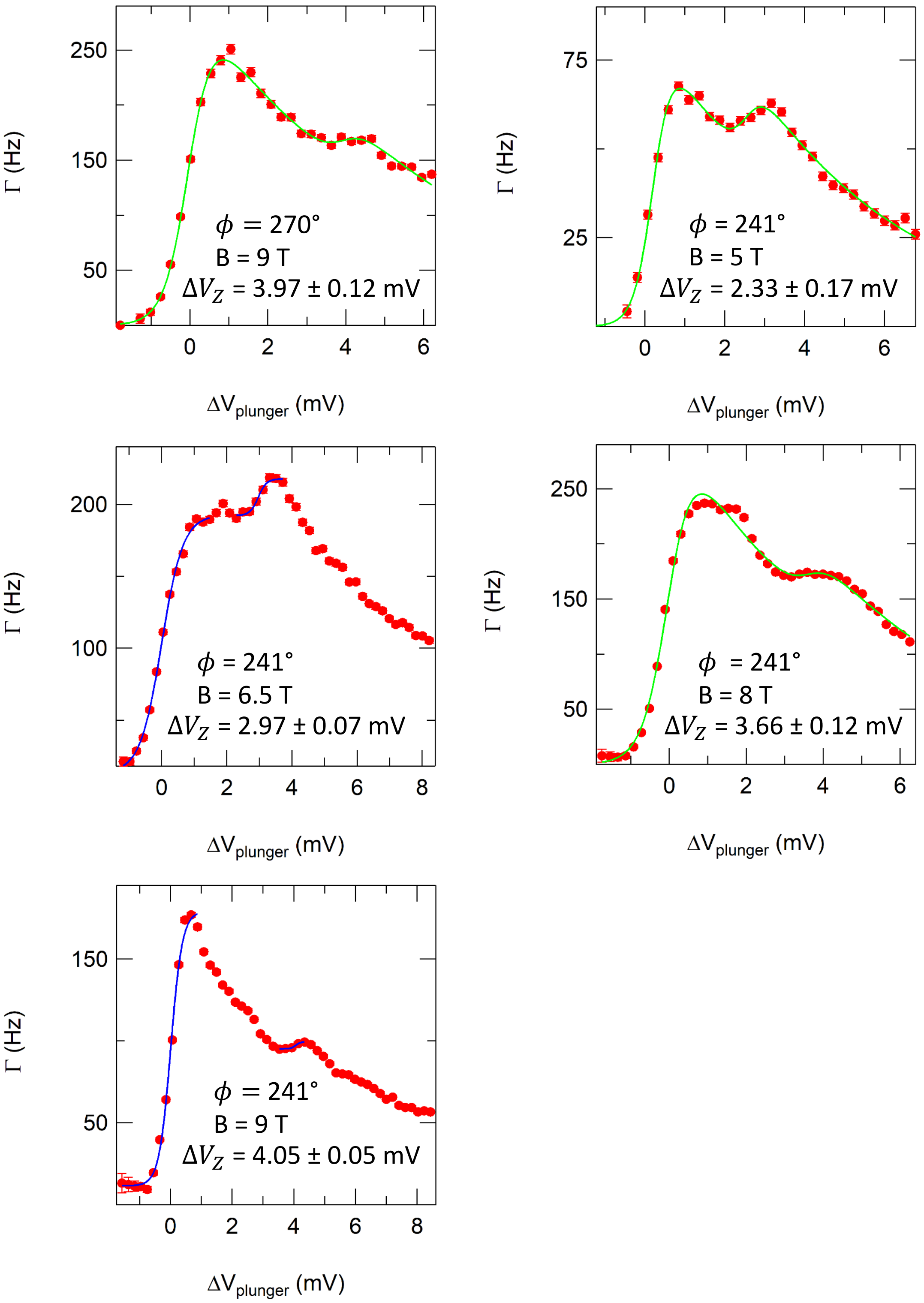

Figure A4: Data set #3 of the tunneling rate Γ in dependence of the pulsed plunger gate voltage $\Delta V_{plunger}$ for in-plane magnetic fields B at different angles ϕ. The voltage difference from the Zeeman splitting ΔV_Z was obtained from fits of either Eq. (19) (green), Eq. (19) with two different factors β (purple) for the two spin states or a sigmoid function (blue, disconnected fits).

A.4 Extracted g-factors for further angles

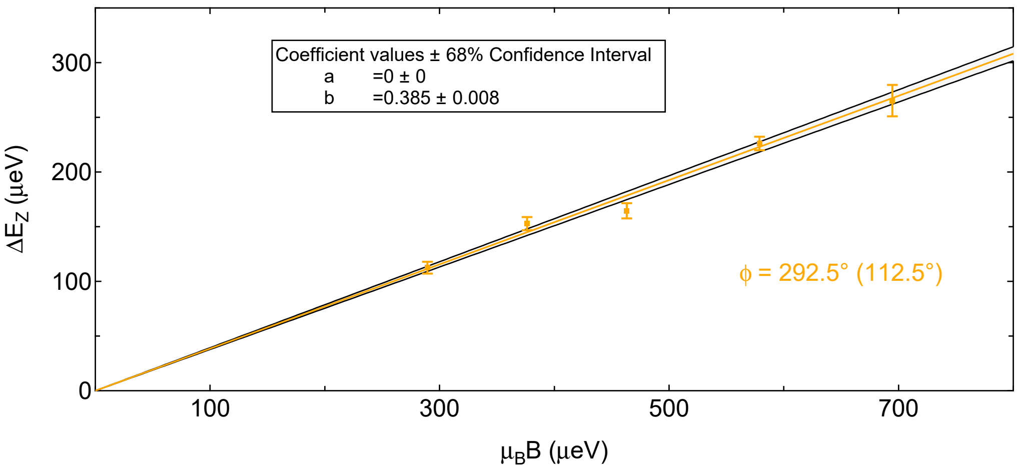

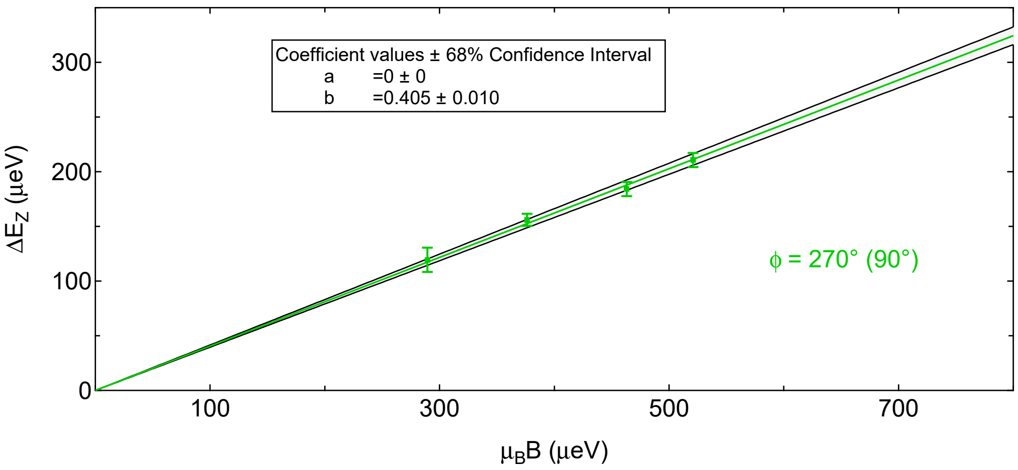

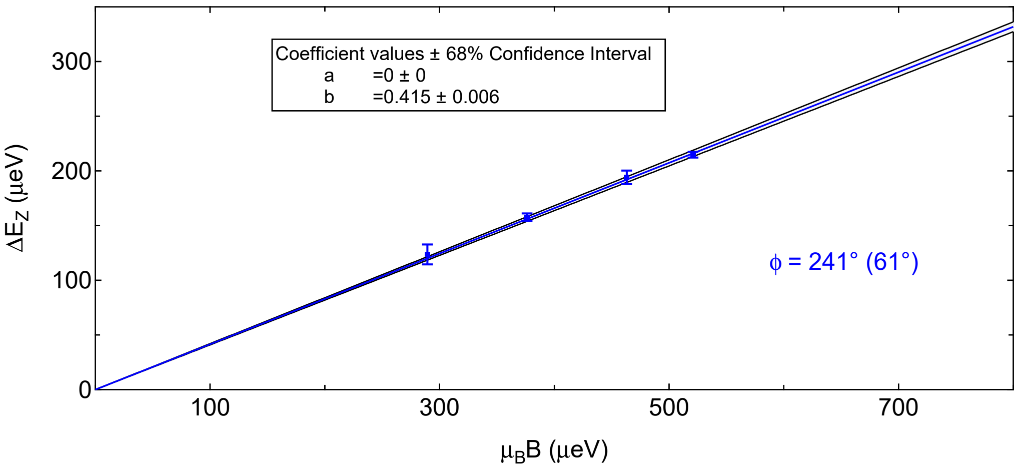

Figure A5: Obtained fits (solid, coloured lines) and extracted absolute g-factor values for in-plane angles $\phi = 292.5°$, $\phi = 270°$ and $\phi = 241°$. The confidence band within one standard deviation is indicated with black lines. Brackets indicate equivalent angles due to the 180°-periodicity of the corrections in ϕ.

A.5 Sinusoidal fit for the calculation of δg_i and δg_a

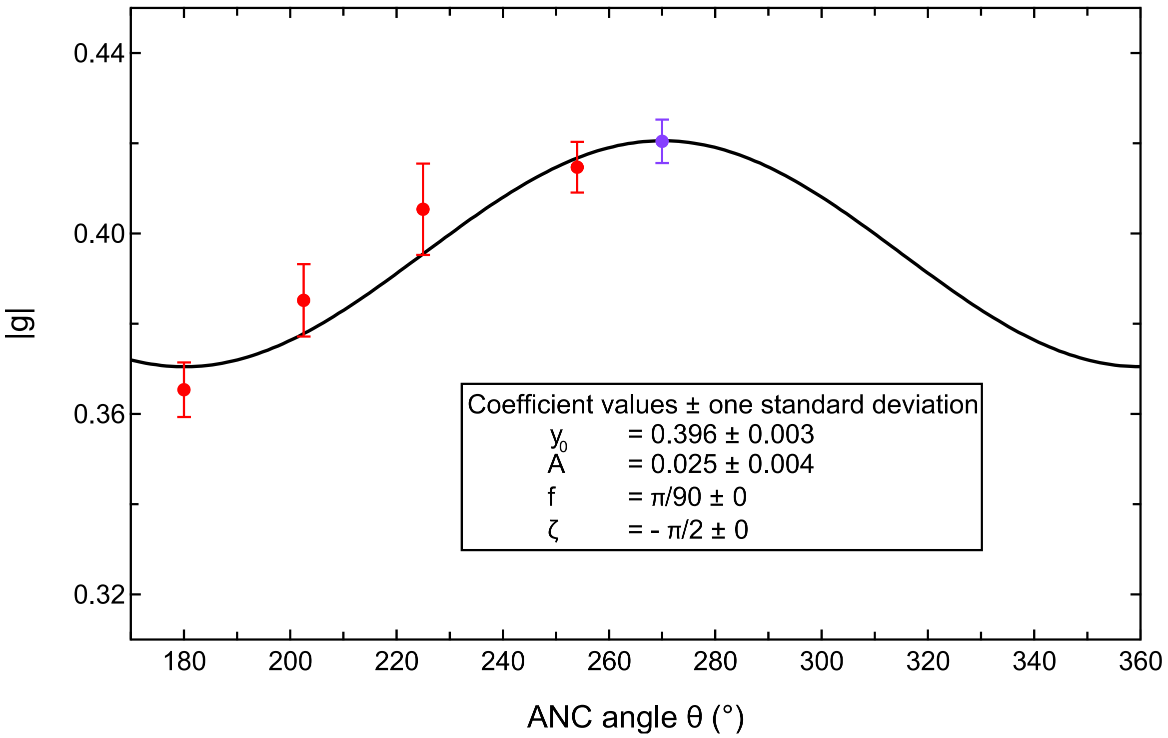

Figure A6: Measured absolute g-factors $|g|$ (dots) in dependence of the angle of the ANC piezo rotator, $\theta = 495° - \phi$. The uncertainties are obtained from the fitting errors. A sine function $y = y_0 + A \cdot sin(f \cdot \theta + \zeta)$ (black curve) is fitted through the data at a fixed frequency and phase, giving a periodicity of 180° and a minimum at $\theta = 180°$. The red data points were measured in this thesis, and the purple data point was measured during its writing process. The offset y_0 is considered to be the absolute value of the mean g-factor, $\bar{g} = g_{bulk} + \delta g_i$, such that $\delta g_i = 0.044 \pm 0.003$ is obtained. The amplitude A is taken as the anisotropic variation, leading to $\delta g_a = 0.025 \pm 0.004$.